

Quantifying the advantages of applying quantum approximate algorithms to portfolio optimisation

Haomu Yuan,^{1,*} Christopher K. Long,¹ Hugo V. Lepage,¹ and Crispin H. W. Barnes¹

¹*Cavendish Laboratory, Department of Physics, University of Cambridge, Cambridge CB3 0HE, UK*

(Dated: October 24, 2024)

We present a quantum algorithm for portfolio optimisation. Specifically, We present an end-to-end quantum approximate optimisation algorithm (QAOA) to solve the discrete global minimum variance portfolio (DGMVP) model. This model finds a portfolio of risky assets with the lowest possible risk contingent on the number of traded assets being discrete. We provide a complete pipeline for this model and analyses its viability for noisy intermediate-scale quantum computers. We design initial states, a cost operator, and ansätze with hard mixing operators within a binary encoding. Further, we perform numerical simulations to analyse several optimisation routines, including layerwise optimisation, utilising COYBLA and dual annealing. Finally, we consider the impacts of thermal relaxation and stochastic measurement noise. We find dual annealing with a layerwise optimisation routine provides the most robust performance. We observe that realistic thermal relaxation noise levels preclude quantum advantage. However, stochastic measurement noise will dominate when hardware sufficiently improves. Within this regime, we numerically demonstrate a favourable scaling in the number of shots required to obtain the global minimum—an indication of quantum advantage in portfolio optimisation.

I. INTRODUCTION

Variational quantum algorithms promise to be powerful tools for approximate optimisation of both classical and quantum problems [1–3]. The Quantum Approximate Optimization Algorithm (QAOA) is one of the most well-known quantum approximate optimisers. It was first introduced to solve binary optimisation problems, MaxCut and MaxSAT, and was then applied to problems in chemistry, quantum field theory, and portfolio optimisation [4–9]. Compared with other applications, quantum portfolio optimisation is arguably the most successful because it relates directly to real-world hedge funds and investment management. Other quantum algorithms have been developed tackling portfolio optimisation with simple models [10–13]. However, many still require validation in the presence of quantum noise and stochastic noise using experiment or simulation. The QAOA has developed applications on more sophisticated portfolio optimisation models with a substantial body of simulations and benchmarks [14–17]. Experiments on current quantum devices suggest that QAOA is capable of reaching a regime where it could challenge the best classical algorithms [18].

After Markowitz introduced the mean-variance portfolio model, portfolio optimisation became an important research field in financial management [19, 20]. However, any departure of the asset return distribution from normality can significantly affect the mean-variance analysis approximation to the optimal portfolio allocation [21]. The complexity and interdependence of global economies make it challenging to predict economic stability, driving investors to pay more attention to portfolio risk. The Global Minimum Variance Portfolio (GMVP) is a known risk-focus portfolio that yielded superior results in many empirical studies [22–25]. However, trading in a practical scenario is usually quantified by discrete numbers of assets because financial products such as stocks, options and futures are not usually infinitely divisible. The DGMVP is the discretisation of the GMVP, in which the number of traded assets is discrete. Therefore, a more efficient method to estimate the DGMVP is of great interest to investors and quantitative analysts.

A mathematical summarisation of the DGMVP model can be written as

$$\underset{\mathbf{w}}{\operatorname{argmin}} f(\mathbf{w}) = \mathbf{w}^\top \Sigma \mathbf{w} \quad (1)$$

$$\text{s.t. } \mathbf{w}^\top \mathbf{1}_n = 1, \quad (2a)$$

$$w_i \in [0, 1], \quad (2b)$$

$$w_i/a \in \mathbb{Z}, \quad i = 1, 2, \dots, n \quad (2c)$$

where $\mathbf{w} = (w_1, w_2, \dots, w_n)^\top$ is an n -dimensional vector of weights for assets $1, \dots, n$, such as stocks, futures, and options, $\mathbf{1}_n$ is an n -dimensional ones vector, and a is the unit trading lot for assets. The $n \times n$ covariance matrix Σ and

* Haomu Yuan hy374@cam.ac.uk

its elements σ_{ij} quantify the risk between each pair of assets. The first constraint Eq. (2a) is the budget constraint, the second constraint Eq. (2b) ensures no short investments, and the third constraint Eq. (2c) is the discretisation. In this article, we will present, to the best of our knowledge, the first end-to-end DGMVP solver based on the QAOA. We design a variational QAOA ansatz and quantify the use of quantum resources. The simulation analysis gives insight into solving other portfolio models and constrained mixed quadratic integer programming with quantum approximate algorithms in the future.

The rest of this article is structured as follows. In Sec. I, we review the original QAOA and general QAOA methods. In Sec. II, we outline a set of QAOA ansatz designs and compare their performance in solving the DGMVP model. In Sec. III, we compare different optimisers and optimisation methods to get the most efficient optimisation strategy. In Sec. IV, we analyse the scaling of the quantum algorithm performance as a function of the asset number and the coarseness of the discretisation and compare it with classical scaling. In Sec. V, we add quantum decoherence noise and apply a post-selection method to improve the approximation. Finally, we conclude in Sec. VI.

REVIEW OF QAOA

Farhi *et al.* first introduced the Quantum Approximate Optimisation Algorithm (the original QAOA) to solve the combinatorial graph problem MaxCut and showed potential advantages [4]. The original QAOA was then generalised by the Quantum Alternating Operator Ansatz (the general QAOA) by redefining a family of cost and mixing operators [5]. To avoid ambiguity, we use the QAOA to represent the general QAOA in the rest of this article, which typically consists of:

1. **Initial state preparation.** We start with a pre-processing step to adjust the zero register to a desired state such as

$$|\text{init}\rangle = U_I |0\rangle^{\otimes n}, \quad (3)$$

where U_I is such a pre-processing operator acting on the $|0\rangle^{\otimes n}$ state. For example, in the MaxCut problem [4], a Hadamard transformation is used to prepare the initial state:

$$U_I = H^{\otimes n}, \quad |\text{init}\rangle = H^{\otimes n} |0\rangle^{\otimes n}, \quad (4)$$

where H is a Hadamard gate. A good initial state will increase the performance of quantum optimisation. Other initial states include the Hartree-Fock [26, 27], Dicke [28], and warm-started states [6, 29]. The warm-started preparation method indicates a strong advantage and beats the GW approximation in solving the MaxCut problem in a low-depth circuit [29].

2. **Cost operator design.** The cost operator $U(C, \gamma)$ is defined such that

$$U(C, \gamma) = e^{-i\gamma C}, \quad (5)$$

where γ is the phase parameter and C is the cost Hamiltonian. The parameter γ is usually restricted by a range. For example, $\gamma \in [0, 2\pi]$ in the MaxCut problem. The cost Hamiltonian C encodes a cost function f , such as the one in Eq. (1), as a series of Pauli-Z strings such that

$$C|z\rangle = f(z)|z\rangle, \quad (6)$$

where $|z\rangle$ is a computational basis state. The cost operator is sometimes named a phase operator because it only generates a phase if acting on a state from the Pauli-Z eigenbasis.

3. **Mixing operator design.** A mixing operator is another parameterised operator alternating with the cost operator. In the MaxCut problem, the authors use a mixing operator $U(B, \beta)$ with B defined by Pauli-X operators:

$$B = \sum_{j=1}^n X_j, \quad U(B, \beta) = e^{-i\beta B} = \prod_{j=1}^n e^{-i\beta X_j}, \quad (7)$$

where $\beta \in [0, \pi]$, n is the the number of qubits, and X_j is the Pauli-X operator acting on the j th qubit. A variety of mixing operators have been developed for a range of problems utilising sophisticated structures and providing other functionalities [5, 30, 31]. The design of mixing operators is becoming a notable research field.

4. **Parameterised alternating ansatz construction.** A parameterised alternating circuit consists of cost operators and mixing operators applied in an alternating fashion to the initial state as shown in Fig. 1. The output state will be

$$|\gamma, \beta\rangle := U(B, \beta_p)U(C, \gamma_p) \dots U(B, \beta_1)U(C, \gamma_1)|S\rangle, \quad (8)$$

where p denotes the number of layers (one mixing operator and one cost operator) of the QAOA, $\gamma = (\gamma_1, \gamma_2, \dots, \gamma_p)$, and $\beta = (\beta_1, \beta_2, \dots, \beta_p)$.

5. **Parameter optimisation.** The parameter array (γ, β) is optimised by an objective function. We utilise the expectation value of the cost Hamiltonian as the objective function, but other common choices are Conditional Value-at-Risk (CVaR), or variance [32, 33]. If we consider a more realistic situation each measurement of the quantum circuit yields a computational basis state $|\mathbf{w}\rangle$ representing a classical value \mathbf{w} . The corresponding cost function value is $f(\mathbf{w})$, and each measurement constitutes a single function access. After k measurements, we can estimate the expectation value of cost Hamiltonian C as

$$\langle C \rangle_k := \langle \gamma, \beta | C | \gamma, \beta \rangle_k = \frac{1}{k} \sum_{i=1}^k f(\mathbf{w}_i). \quad (9)$$

where such an estimation uses k function accesses. Classical optimisers are used to optimise the cost and mixing operators' parameters [9, 34–37].

II. QUANTUM OPTIMISATION METHODS

In this section, we first binary-encode the weight vector \mathbf{w} . Then, this section presents the three main elements of the QAOA within the encoding: initial states, a cost operator, and a hard mixing operator.

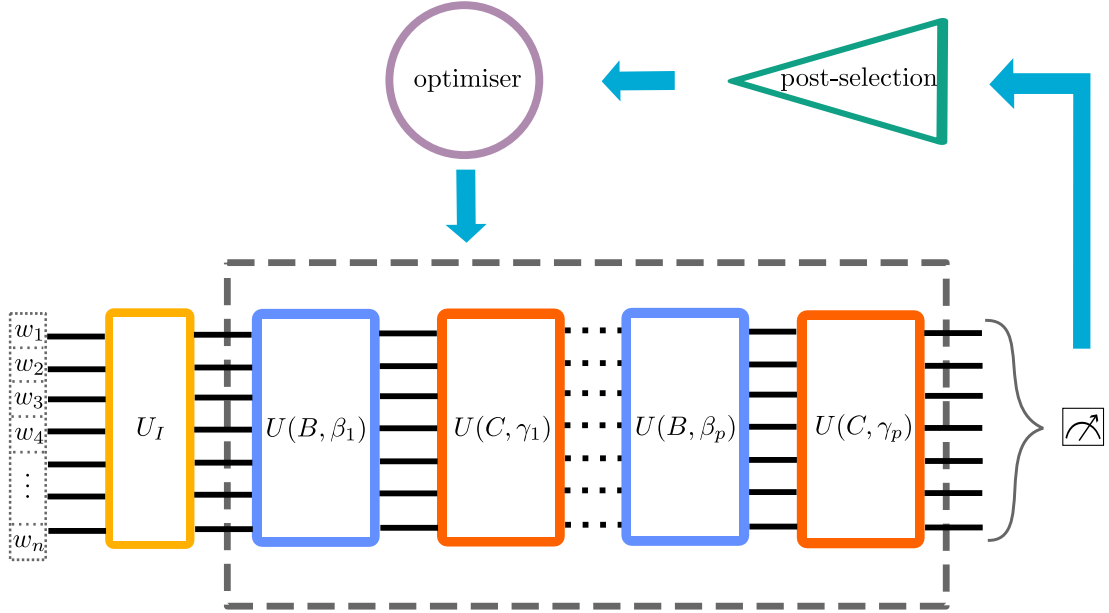


Figure 1. A parameterised QAOA ansatz for predicting the DGMVP solution. The variables w_1, w_2, \dots, w_n in the dotted squares are the binary-encoded weight variables. The unitary U_I prepares the initial state. The grey dashed box includes the mixing ($U(B, \beta)$) and cost ($U(C, \gamma)$) operators. A tunable parameter controls each operator. After measurements, a post-selection process will be applied to filter out unconstrained results and feed them to the classical optimiser.

A. Binary block encoding method

In previous quantum portfolio optimisation algorithms [6, 11, 14], the authors encode at most three trading positions (long, short, and on-hold) with two binary variables by treating the first variable as a long position and the second as

a short position. However, the DGMVP and most portfolio strategies usually require an encoding with more positions encoded as multiples of the unit trading lot a . A quasi-binary encoding method provided in [17] uses a large enough factor $1/a$ to amplify all weights variables to integers. This article uses a binary encoding method with a fixed length for all assets.

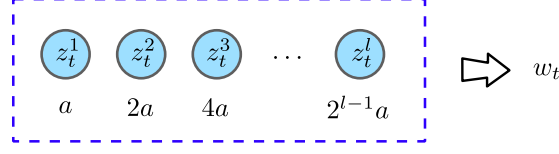


Figure 2. A diagram of binary block encoding for the t th asset investment weight w_t . The circles represent binary variables $z_t^1, z_t^2, \dots, z_t^l$ from measuring qubits on the Pauli-Z basis. The weight of variables $a, 2a, \dots, 2^{l-1}a$ are shown at the bottom of the corresponding variables circles. Each w_t combines an l length block of binary variables from the measurement of qubits.

The variable w_t can be encoded with a block of l binary variables (see Fig. 2),

$$w_t = \sum_{k=1}^l b^k z_t^k, \quad (10)$$

where $z_t^k \in \{0, 1\}$ is a binary variable corresponding to the measurement of a qubit state in Pauli-Z basis, and b^k is

$$b^k = 2^{k-1}a, \quad (11)$$

where a is the binary precision and can be interpreted as the unit trading lot:

$$a = \frac{1}{\sum_{i=0}^{l-1} 2^i} = \frac{1}{2^l - 1}. \quad (12)$$

Then, the total number of shares is $1/a$. As block sizes increase, the binary encoding method will use exponentially fewer qubits than the one-hot encoding method [38].

B. Initial state preparations

A good design of an initial state for target applications can avoid initialising far away from the global optimum and reduce the convergence time in quantum optimisation [6, 29]. This article provides four initial state preparation methods for the DGMVP model: max-biased state, ranked warm-started state, approximated equal-weighted state, and random-weighted state. Experiments in Appx. C show max-biased state and ranked warm-started state outperform other methods. Thus, we focus on these two methods in the body and summarise the rest of the initial states in the Appx. C.

The max-biased state $|\mathbf{w}\rangle_{mb}$:—This state represents an all-in-one investment without diversification, as

$$w_t = \begin{cases} 1, & t = a \\ 0, & t \neq a. \end{cases} \quad (13)$$

The ranked warm-started state $|\mathbf{w}\rangle_{ws}$:—This state represents an approximation to the DGMVP solution from the round-off of the GMVP model's continuous solution $\tilde{\mathbf{w}}$. The values in $\tilde{\mathbf{w}}$ can be divided by the binary precision a to get sets of reminders $\tilde{\mathbf{r}}$ and divisors $\tilde{\mathbf{z}}$:

$$\tilde{z}_i = \left\lfloor \frac{\tilde{w}_i}{a} \right\rfloor, \quad \tilde{r}_i = \frac{\tilde{w}_i}{a} - \left\lfloor \frac{\tilde{w}_i}{a} \right\rfloor, \quad \forall \tilde{w}_i \in \tilde{\mathbf{w}}. \quad (14)$$

Further, we define the remaining budget $u := 1/a - \sum_{\tilde{z}_i \in \tilde{\mathbf{z}}} \tilde{z}_i$. First, we order the assets from the largest value \tilde{r}_i to the smallest. Then, we assign the remaining budget one-by-one to the first u assets. A ranked warm-started state $|\mathbf{w}\rangle_{ws}$ of the DGMVP model prepares the asset weights as

$$w_i = \begin{cases} a\tilde{z}_i + a, & i \leq u \\ a\tilde{z}_i, & i > u \end{cases}. \quad (15)$$

C. The design of cost Hamiltonian and cost operator for the DGMVP model

This section introduces the construction of the cost Hamiltonian C for the DGMVP model, the corresponding cost operator, and the quantum circuit. Using the binary block encoding from Sec. II A, the DGMVP problem in Eq. (1) can be rewritten as

$$\begin{aligned} \underset{\mathbf{x}}{\text{argmin}} \quad & f = a^2 \sum_{i,j} \sigma_{ij} x_i x_j \\ \text{s.t.} \quad & \sum_i a x_i = 1, \\ & 0 \leq x_i \leq D, \quad x_i \in \mathbb{Z} \end{aligned} \quad (16)$$

where \mathbf{x} is a n dimensional vector with elements $x_i = w_i/a = \sum_{k=1}^l b^k z_i^k$ (see in Sec. II A) and $D = 1/a$. Substituting for the w_i we find

$$f = 2a^2 \sum_{i < j} \sum_{k_1, k_2} \sigma_{ij} b^{k_1} z_i^{k_1} b^{k_2} z_j^{k_2} + a^2 \sum_i \sum_{k_1, k_2} \sigma_{ii} b^{k_1} z_i^{k_1} b^{k_2} z_i^{k_2}. \quad (17)$$

Using the relations

$$\frac{1-Z}{2}|0\rangle = 0|0\rangle, \quad \frac{1-Z}{2}|1\rangle = 1|1\rangle, \quad (18)$$

where Z is a Pauli-Z operator and $\mathbb{1}$ is the identity operator, and Eq. (5), the Hamiltonian C can be written as

$$\begin{aligned} C = & \frac{a^2}{2} \sum_{i < j} \sum_{k_1, k_2} \sigma_{ij} b^{k_1} b^{k_2} \left(Z_i^{k_1} Z_j^{k_2} - Z_i^{k_1} - Z_j^{k_2} + \mathbb{1} \right) \\ & + \frac{a^2}{4} \sum_i \sum_{k_1, k_2} \sigma_{ii} b^{k_1} b^{k_2} \left(Z_i^{k_1} Z_i^{k_2} - Z_i^{k_1} - Z_i^{k_2} + \mathbb{1} \right), \end{aligned} \quad (19)$$

where Z_i^k is the Pauli-Z operator on the k th qubit of the i th asset. Since every weight operator use the same number of binary variables for the encoding, then

$$\frac{a^2}{4} \sum_i \sum_{k_1, k_2} \sigma_{ii} b^{k_1} b^{k_2} Z_i^{k_2} = \frac{a^2}{4} \sum_i \sum_{k_1, k_2} \sigma_{ii} b^{k_1} b^{k_2} Z_i^{k_1} \quad (20)$$

and

$$\begin{aligned} & \frac{a^2}{2} \sum_{i < j} \sum_{k_1, k_2} \sigma_{ij} b^{k_1} b^{k_2} Z_i^{k_1} + \frac{a^2}{2} \sum_{i < j} \sum_{k_1, k_2} \sigma_{ij} b^{k_1} b^{k_2} Z_j^{k_2} + \frac{a^2}{2} \sum_i \sum_{k_1, k_2} \sigma_{ii} b^{k_1} b^{k_2} Z_i^{k_2} \\ = & \frac{a^2}{2} \sum_{i < j} \sum_{k_1, k_2} \sigma_{ij} b^{k_1} b^{k_2} Z_i^{k_1} + \frac{a^2}{2} \sum_{j < i} \sum_{k_1, k_2} \sigma_{ij} b^{k_1} b^{k_2} Z_i^{k_1} + \frac{a^2}{2} \sum_i \sum_{k_1, k_2} \sigma_{ii} b^{k_1} b^{k_2} Z_i^{k_1} \\ = & \frac{a^2}{2} \sum_{i,j} \sum_{k_1, k_2} \sigma_{ij} b^{k_1} b^{k_2} Z_i^{k_1} = \frac{a^2}{2} \sum_{i,j} \sum_{k_2} b^{k_2} \sum_{k_1} \sigma_{ij} b^{k_1} Z_i^{k_1} = \frac{a^2}{2} \sum_{i,j} \frac{1}{a} \sum_{k_1} \sigma_{ij} b^{k_1} Z_i^{k_1} \\ = & \frac{a}{2} \sum_i \sum_k \tilde{\sigma}_i b^k Z_i^k, \end{aligned} \quad (21)$$

where the second equality comes from the symmetry $\sigma_{ij} = \sigma_{ji}$, and $\tilde{\sigma}_i = \sum_j \sigma_{ij}$. By substituting the Eqs. (20) and (21) into Eq. (19), the DGMVP Hamiltonian C can be expressed as

$$C = \frac{a^2}{2} \sum_{i < j} \sum_{k_1, k_2} \sigma_{ij} b^{k_1} b^{k_2} Z_i^{k_1} Z_j^{k_2} + \frac{a^2}{4} \sum_i \sum_{k_1 \neq k_2} \sigma_{ii} b^{k_1} b^{k_2} Z_i^{k_1} Z_i^{k_2} - \frac{a}{2} \sum_i \sum_k \tilde{\sigma}_i b^k Z_i^k + c, \quad (22)$$

where c is a constant scalar, the $k_1 \neq k_2$ condition in the second term is derived from $Z_i^{k_1} Z_i^{k_2} = 1$ when $k_1 = k_2$. We can drop the constant offset c because it can be considered as a global phase. The cost operator of the DGMVP Hamiltonian C is

$$\begin{aligned} U(C, \gamma) &= e^{-i\gamma C} \\ &= \prod_{i < j} \prod_{k_1, k_2} e^{-\frac{i\gamma a^2}{2} \sigma_{ij} b^{k_1} b^{k_2} Z_i^{k_1} Z_j^{k_2}} \prod_i \prod_{k_1 \neq k_2} e^{-\frac{i\gamma a^2}{4} \sigma_{ii} b^{k_1} b^{k_2} Z_i^{k_1} Z_i^{k_2}} \prod_i \prod_k e^{\frac{i\gamma a}{2} \tilde{\sigma}_i b^k Z_i^k}, \end{aligned} \quad (23)$$

where $\gamma \in [0, 2\pi]$. We can separate the products of exponentials because Pauli-Z strings commute with each other. Eq. (23) contains both singular and coupling Pauli-Z strings—the corresponding digital quantum circuit is shown in Fig. 3(a)(b), respectively. As the covariance matrix Σ is dense, coupling Pauli-Z strings in $U(C, \gamma)$ will contain interactions between all pairs of qubits. Thus, a dense quantum circuit can be constructed with $\mathcal{O}(N)$ depth, where N is the number of qubits [39, 40].

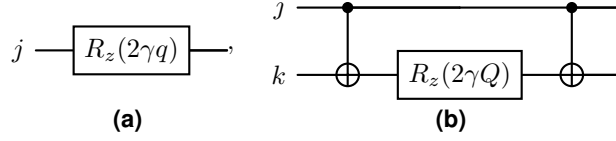


Figure 3. (a) Cost operator circuit design of $e^{-i\gamma q Z_j}$. (b) Cost operator circuit design of $e^{-i\gamma Q Z_j Z_k}$.

D. Hard mixing operator based on qubit excitations

In this section, we design a hard mixing operator based on the qubit excitation operators to conserve the budget constraint in the QAOA optimisation. There are two types of mixing operators in the current quantum portfolio solvers: *Hard mixing operators* and *soft mixing operators*. Hard mixing operators, unlike soft mixing operators, obey the problem constraints. In Appx. B, we show the gap between the constrained and unconstrained feasible region size scales exponentially. This gap may imply that soft mixing operators can induce significant measurement overheads to optimisation. Hodson *et al.* designed the *parity mixer*, a hard mixing operator, alternating the application of Pauli-XY mixers to the odd and even spin subsets, representing short and long positions, respectively [14]. Their simulations show that the parity mixer outperforms the standard QAOA soft mixing operator in portfolio rebalancing. Chen *et al.* extended the design of the parity mixer as the *ring mixer* by adding Pauli-XY mixers to solve a quasi-binary encoded problem [17]. Our algorithm includes a hard mixing operator design constructed using two- and three-qubit excitation operators and the induced quantum bridge phenomenon introduced in Appcs. D and E.

In principle, within the binary encoding of the DGMVP model, a combination of two binary arithmetic operations can reach all constrained \mathbf{w} . The first operation, *exchange*, swaps excited qubits representing the variables with the same binary coefficient, such as z_t^k and $z_{t'}^k$, where z_t^k and $z_{t'}^k$ are the k th qubits in the t and t' asset blocks of the binary block encoding. This conserves the total number of excited qubits. The exchange operation includes two transformations:

$$\begin{cases} (1, 0) \mapsto (0, 1) \\ z_t^k \quad z_{t'}^k \quad z_t^k \quad z_{t'}^k \\ (0, 1) \mapsto (1, 0) \\ z_t^k \quad z_{t'}^k \quad z_t^k \quad z_{t'}^k \end{cases}. \quad (24)$$

The other operation is the *carry-borrow* operation and includes transformations as follows:

$$\begin{cases} (0, 1, 1) \mapsto (1, 0, 0) \quad \text{carry} \\ z_t^{k+1} \quad z_{t'}^k \quad z_{t''}^k \quad z_t^{k+1} \quad z_{t'}^k \quad z_{t''}^k \\ (1, 0, 0) \mapsto (0, 1, 1) \quad \text{borrow} \\ z_t^{k+1} \quad z_{t'}^k \quad z_{t''}^k \quad z_t^{k+1} \quad z_{t'}^k \quad z_{t''}^k \end{cases}, \quad (25)$$

where assets label $t' \neq t''$. The carry in the quantum setup corresponds to exciting a qubit at binary position $k+1$ and de-exciting two other qubits at binary position k , and the borrowing process is the reverse direction.

From [41], a two-qubit excitation operator can perform the operation in Eq. (24) and is defined as

$$S_{tt'}^{k\dagger} := Q_{t'}^{k\dagger} Q_t^k - Q_{t'}^k Q_t^{k\dagger}, \quad (26)$$

where

$$Q_t^{k\dagger} = \frac{1}{2}(X_t^k - iY_t^k), \quad Q_t^k = \frac{1}{2}(X_t^k + iY_t^k), \quad (27)$$

and X_t^k and Y_t^k are the Pauli-X and Pauli-Y operators acting on k th qubit of the t th asset. The operation in Eq. (25) can be achieved by the three-qubit excitation operator

$$P_{tt't''}^k := Q_t^{k+1\dagger} Q_t^k Q_{t'}^k - Q_t^{k+1} Q_t^{k\dagger} Q_{t'}^{k\dagger}, \quad (28)$$

where assets label $t' \neq t''$. The two parameterised evolution unitaries are

$$\begin{aligned} e^{\beta S_{tt'}^k} &= \cos^2 \frac{\beta}{2} \mathbb{1} + \sin^2 \frac{\beta}{2} Z_t^k Z_{t'}^k + \sin \beta S_{tt'}^k, \\ e^{\beta P_{tt't''}^k} &= \frac{1}{4} (3 + \cos(\beta)) \mathbb{1} + \frac{1}{2} \sin^2 \left(\frac{\beta}{2} \right) (Z_t^{k+1} Z_{t'}^k + Z_t^{k+1} Z_{t''}^k - Z_t^k Z_{t'}^k) + \sin(\beta) P_{tt't''}^k, \end{aligned} \quad (29)$$

where $\beta \in [0, 2\pi]$ and the corresponding quantum circuit design is shown in Fig. 4. Thus, $e^{\beta S_{tt'}^k}$ has support on $\mathbb{1}$, $Z_t^k Z_{t'}^k$, and the two-qubit excitation operators $S_{tt'}^k$. Additionally, $e^{\beta P_{tt't''}^k}$ has support on $\mathbb{1}$, $Z_t^{k+1} Z_{t'}^k$, $Z_t^{k+1} Z_{t''}^k$, $Z_t^k Z_{t'}^k$, and the three-qubit excitation operator $P_{tt't''}^k$. The $\mathbb{1}$ leaves the state invariant. The Pauli-Z strings generate phases between computational basis states. The qubit excitation operators, $S_{tt'}^k$ and $P_{tt't''}^k$, perform the binary arithmetic operations in Eqs. (24) and (25). The support on the qubit excitation operators changes the occupation of computational basis states while still obeying the constraints in Eqs. (2a) to (2c). The parameter β controls the degree of superposition, performing optimisation improves the superposition to a better approximation. In Fig. 5 (a) and (b), we present two graphs that represent the support of the two- and three-qubit excitations, respectively.

Furthermore, if we compose the two- and three-qubit excitation operators as follows:

$$e^{\beta S_{tt'}^{k'}} e^{\beta P_{ttt'}^{k'}} e^{\beta S_{tt'}^{k'}}, \quad (30)$$

it will also include the support of qubit excitation operators of $e^{\beta P_{tt't}^{k'}}$ as shown from Fig. 5 (c) to (d) due to a phenomenon we denote as the *quantum bridge* outlined in Appx. E. Thus, by stacking qubit excitations, the composition

$$\begin{aligned} &\left(\bigotimes_{i=k'k''} e^{\beta S_{tt'}^i} \right) \left(e^{\beta P_{ttt'}^{k'}} e^{\beta P_{ttt''}^{k''}} \right) \left(\bigotimes_{i=k',k''} e^{\beta S_{tt'}^i} \right) \\ &= \left(e^{\beta S_{tt'}^{k'}} e^{\beta P_{ttt'}^{k'}} e^{\beta S_{tt'}^{k'}} \right) \left(e^{\beta S_{tt'}^{k''}} e^{\beta P_{ttt''}^{k''}} e^{\beta S_{tt'}^{k''}} \right), \end{aligned} \quad (31)$$

has support on all two- and three-qubit excitation operators between qubits sub-systems $z_t^{k'}$, $z_{t'}^{k'}$, $z_t^{k''}$, and $z_{t'}^{k''}$ — Eq. (31) is derived in Appx. F.

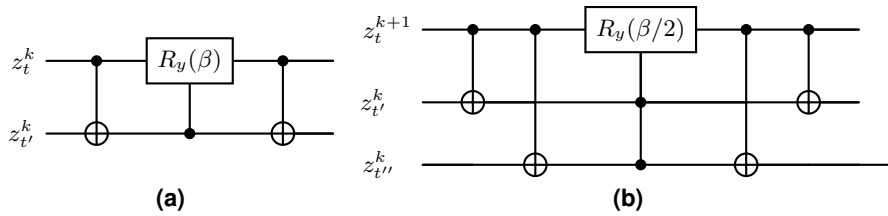


Figure 4. Quantum circuit design for (a) $e^{\beta S_{tt'}^k}$ and (b) $e^{\beta P_{tt't''}^k}$.

By extending this stacked structure consisting of four layers, we can construct a circuit of constant depth with support on all the generators of two- and three-qubit excitations that correspond to valid binary arithmetic operations between assets t and t' :

$$H_{tt'}(\beta) = \tilde{S}_{tt'}(\beta) \tilde{P}_{tt'}^e(\beta) \tilde{P}_{tt'}^o(\beta) \tilde{S}_{tt'}(\beta), \quad (32)$$

where

$$\begin{aligned} \tilde{S}_{tt'}(\beta) &= \bigotimes_{k=1}^l e^{-i\beta S_{tt'}^k}, \\ \tilde{P}_{tt'}^e(\beta) &= \bigotimes_{k_1 \in \mathcal{K}_1} e^{-i\beta P_{ttt'}^{k_1}}, \quad \mathcal{K}_1 = \{(2c_1) \bmod l, c_1 = 1, 2, \dots, \lfloor l/2 \rfloor\}, \\ \tilde{P}_{tt'}^o(\beta) &= \bigotimes_{k_2 \in \mathcal{K}_2} e^{-i\beta P_{ttt''}^{k_2}}, \quad \mathcal{K}_2 = \{(2c_2 - 1) \bmod l, c_2 = 1, 2, \dots, \lfloor l/2 \rfloor\}, \end{aligned} \quad (33)$$

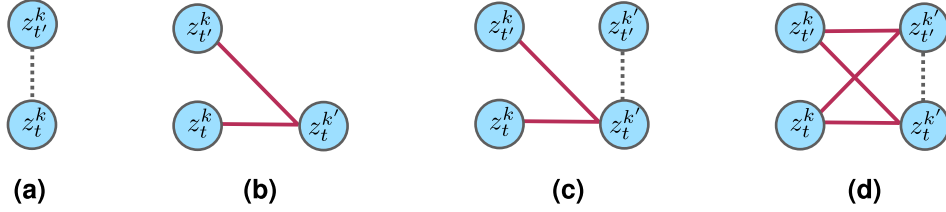


Figure 5. Graphs representing the composition of qubit excitations. The nodes represent the qubits acted upon non-trivially. The edges represent support of the resultant unitary on the generators of two- (dash) and three-qubit excitations (solid). (a) The unitary $e^{\beta S_{tt'}}$ generated by the two-qubit excitation. (b) The unitary $e^{\beta P_{ttt'}}$ generated by the three-qubit excitation. (c) The union of the support of the unitaries $e^{\beta S_{tt'}}$, $e^{\beta P_{ttt'}}$, and $e^{\beta S_{tt'}}$ generated by two- and three-qubit excitations. (d) The composition $e^{\beta S_{tt'}} e^{\beta P_{ttt'}} e^{\beta S_{tt'}}$ also includes support on $P_{t'tt}$ due to the quantum bridge—see Appx. E.

see Appx. F for details. The graph of the support of $H_{tt'}(\beta)$ on the generators of two- and three-qubit excitations is as shown in Fig. 6.

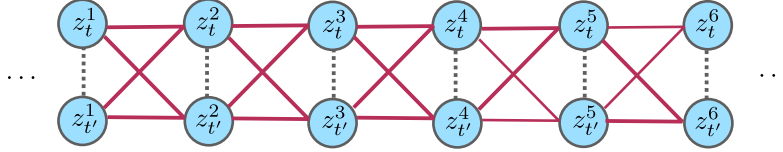


Figure 6. A graph representing the composition $H_{tt'}(\beta)$ of qubit excitations. The nodes represent the qubits acted upon non-trivially. The edges represent the support of the resultant unitary on the generators of two- (dash) and three-qubit excitations (solid).

We can then define a hard mixing operator as

$$\hat{M}_L(\beta) = \prod_{d=1}^L \prod_{tt'} H_{tt'}(\beta), \quad |t - t'| \bmod n = d, \quad 1 \leq L \leq \lfloor n/2 \rfloor, \quad (34)$$

where L represents the maximum distance between assets. Assuming all-to-all qubit connectivity the depth complexity is $\mathcal{O}(L)$. If we set $L = 1$, a nearest-neighbour hard mixing operator is

$$\hat{M}_1(\beta) = \prod_{tt'} H_{tt'}(\beta), \quad |t - t'| \bmod n = 1. \quad (35)$$

When choosing $L = \lfloor n/2 \rfloor$, the mixing operator will contain qubit excitations between all pairs of assets. In the following sections, unless stated, we use $\hat{M}_1(\beta)$ as the mixing operator due to its better performance in the optimisation (see Appx. G) and the minimal use of quantum gates. Further, by repeatedly applying $\hat{M}_L(\beta)$ interleaved with cost operators in the QAOA ansatz, we generate *long-exchange*, *-carry* and *-borrow* operations between assets through transporting excitation from neighbour to neighbour.

III. PARAMETERISED CIRCUIT OPTIMISATION

This section benchmarks two classical parameter optimisers, Dual Annealing (DA) and Constrained Optimisation by Linear Approximation (COBYLA) [42, 43], and two layerwise optimisation methods, *frozen-layerwise* and *unfrozen-layerwise* for our QAOA ansatz.

Optimisation of our ansatz is governed primarily by two hyperparameters which we will consider in turn below: The number of shots N_m used to calculate expectation values and the maximum number of expectation values that can be estimated by the optimiser \mathcal{I} .

As with most QAOA applications, our simulations use the estimation of an expectation value $\langle C \rangle_{N_m}$ using N_m (optimisation) shots as the objective function. We observe in Fig. 7 that insufficient shots will lead to a sizeable stochastic noise and an unstable optimisation. We use $N_M \geq N_m$ (post-optimisation) shots to obtain a more precise

estimation of the expectation value of a post-optimised quantum circuit. A further discussion about the effect of different N_m on optimisation is given in Sec. III A.

From our simulations, we also find classical optimisers sometimes fail to identify convergence (see left column of Fig. 7) due to the poor loss landscape of the quantum circuit and stochastic measurement noise. Thus, employing an \mathcal{I} is important to limit the overuse of resources. Finally, we denote the total number of objective functions assessed during the optimisation as N_f —which is determined by N_m and \mathcal{I} .

To evaluate the efficacy of a QAOA after optimisation, a common metric is the mean value approximation ratio:

$$\alpha_{\text{mean}} = \frac{\langle C \rangle_{N_M} - f_{\min}}{f_{\max} - f_{\min}}, \quad (36)$$

where $\langle C \rangle_{N_M}$ is defined in Eq. (9), f_{\min} and f_{\max} are the global minimal and maximal values of the cost function [Eq. (1)], respectively. α_{mean} is normalised within the range $[0, 1]$. Unlike the approximation ratio in the maxcut problem, our approximation ratio is better when it's lower. However, the portfolio strategy with the global optimum that a solver can find is more useful for the DGMVP model, so we also introduce the minimal value approximation ratio:

$$\alpha_{\min} = \frac{\min_{i \in [1, N_M]} \{ \langle \mathbf{w}_i | C | \mathbf{w}_i \rangle \} - f_{\min}}{f_{\max} - f_{\min}}, \quad (37)$$

where the \mathbf{w}_i is the i th measured weight vector.

A. Classical optimisers

DA is a stochastic global optimisation method that couples a local search with simulated annealing. COBYLA is a derivative-free local optimisation method to approximate constrained optimisation problems with linear programming problems iteratively. Benchmarks demonstrate that COBYLA can converge to lower energies faster than other local optimisers when optimising variational quantum algorithms in the absence of noise [44, 45].

In Fig. 7, we use the COBYLA and DA to optimise one ansatz parameter for different numbers of measurement shots N_m during the optimisation, fixing the DGMVP instance and keeping other ansatz parameters the same. The simulation demonstrates the difficulty of classical optimisers when optimising the loss landscape in the presence of stochastic noise [46]. This is particularly evident for COBYLA (see left-hand column of Fig. 7): as the number of optimisation shots N_m decreases, COBYLA starts to terminate the optimisation at a stochastically generated position as opposed to a local minimum. Although a sufficiently large N_m can be helpful to the optimisation, it will also lead to excessive cost function accesses, diminishing the advantage of quantum algorithms. Fortunately, we observe a better result for DA (see right-hand column of Fig. 7): a stable performance in finding a point near the global minimum as N_m is reduced with a constant number of expectation value estimations. Notably, even when decreasing the optimisation shots drastically, as shown in the bottom-right panel of Fig. 7, DA still stops at a region close to the optimal parameter. However, DA will fail to identify convergence at the end of optimisation due to stochastic noise, and an \mathcal{I} should be set to avoid the over-optimisation cost.

Furthermore, a set of simulations in Appx. H shows the advantages of using DA over COBYLA to optimise multi-layered ansätze in the presence of stochastic measurement errors. In Appx. I, we also consider DA for a range of \mathcal{I} and N_m and determine a reasonable choice as $\mathcal{I} = 2000$ and $N_m = 16$, which we employ in Sec. IV.

B. Layerwise optimisation

Layerwise optimisation is becoming a popular optimisation method for the QAOA and indicates faster convergence in many simulations [47–50]. There are many variant versions of the layerwise optimisation methods, and they can be categorised as frozen-layerwise and unfrozen-layerwise for our ansatz. For a fixed $p > 1$, both methods start with optimising the $p' = 1$ circuit with random initial parameters and store the optimised parameters as γ', β' . Then, we add subsequent layers by setting the previous layers' parameters as γ', β' and initialising the new layer's parameters as zero (an identity layer) to avoid detrimenting the prior optimisation. On the one hand, in frozen-layerwise optimisation, we fix parameters from before the new layer is added and only optimise the parameters in the new layer. On the other hand, in unfrozen-layerwise optimisation, we optimise all of the layers' parameters together. For both methods, a well-optimised p layer quantum circuit can then be iteratively constructed by adding a new layer and optimising. When using DA as the layerwise optimiser, we limit the number of expectation value estimations

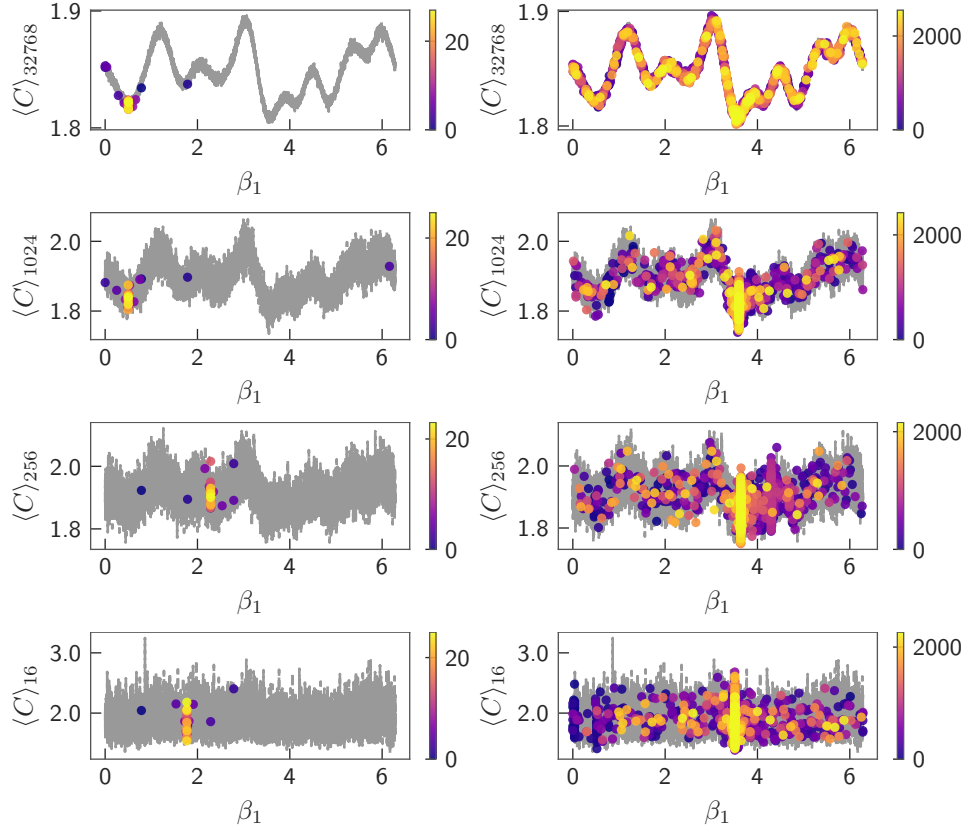


Figure 7. The performance of COBYLA (left column) and DA (right column) when optimising β_1 with other parameters fixed. These simulations use $n = 4$ assets, an asset encoding binary block length of $l = 4$, a QAOA circuit with $p=10$ layers and $\hat{M}_2(\beta)$ as the mixing operator, and $|\mathbf{w}\rangle_{mb}$ as the initial state. The loss landscape based on sampling from the cost function of β_1 with stochastic noise is plotted as grey lines. For DA, we use $\mathcal{I} = 2000$ as the maximal number of expectation value estimations. The level of stochastic noise increases down the page. That is the number of shots utilised for sampling is $N_m=2^{15}$, 2^{10} , 2^8 and 2^4 from the top row to the bottom. The overlaid coloured points indicate the values of the cost function sampled by the optimiser at each step during the optimisation. The colour bar on the right indicates the optimisation steps.

used during optimisation after adding each new layer to \mathcal{I}' . Thus, after adding a total of p layers, the maximum number expectation value estimations is $\mathcal{I} = \mathcal{I}'p$.

In Fig. 8, we perform a comparison of the unfrozen-layerwise, the frozen-layerwise, and the fix ansatz approach optimisation methods with COBYLA and DA to a fixed DGMVP instance with a fixed number of measurement shots $N_m = 1024$ during the optimisation. The simulation shows that unfrozen-layerwise optimisation, in general, outperforms frozen-layerwise in both α_{mean} and α_{min} . The value of α_{mean} after optimisation is roughly constant after $p = 2$ for both layerwise methods with COBYLA and DA. In the COBYLA simulations [see Fig. 8(a)], we observe a lower α_{mean} for both layerwise methods compared to the fixed ansatz approach. Furthermore, for the DA simulations, the unfrozen-layerwise optimisation in Fig. 8(c) uses the same number of expectation value estimations in total but achieves a better result than the fix ansatz approach for circuits with larger p . In Fig. 8(b) and (d), the median of α_{min} is pinned at zero for all methods but frozen-layerwise with DA at almost all p —at least 50% of the time the true global minimum is found. Thus, we plot the 80% percentile to indicate the tail of the distribution. When using COBYLA, we observe that the fix ansatz approach gives the tightest distribution for the larger p circuits. Further, we find that the unfrozen-layerwise approach using DA returns the global minimum with a probability greater than 80% for $p \geq 3$ and outperforms all other methods presented. Compared to optimising the p layer circuit directly as in the fix ansatz approach, the unfrozen-layerwise optimisation also uses a shorter circuit until adding the last layer which reduces quantum resource usage. The layerwise methods may also be more noise-robust by minimising the noise induced by finite coherence times during the early stages of optimisation.

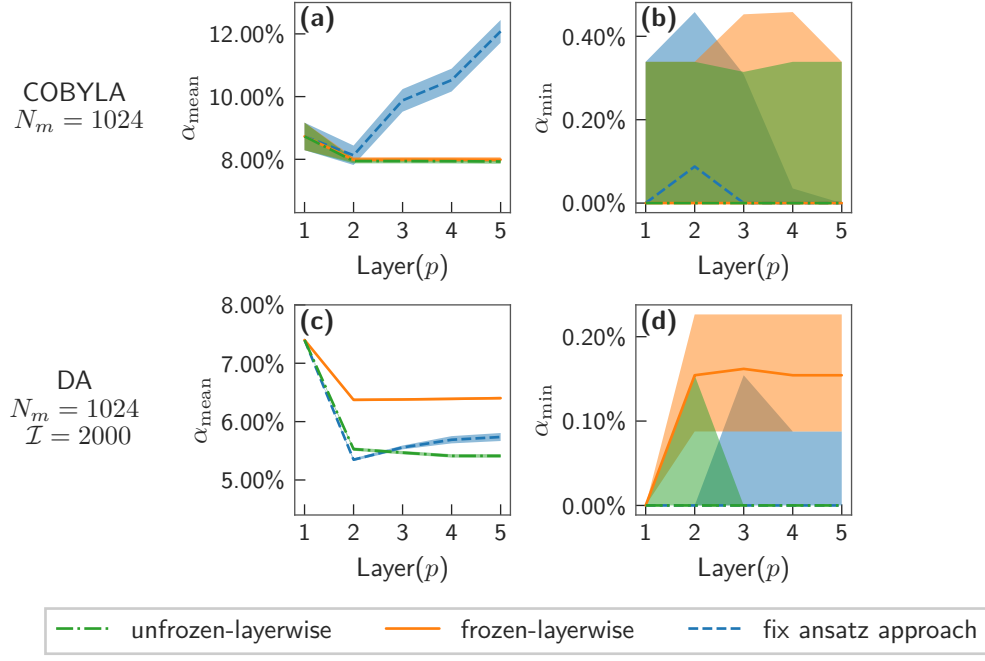


Figure 8. A comparison of optimisation methods: (a)(b) use COBYLA as the optimiser with $N_m = 1024$; (c)(d) use DA as the optimiser with $\mathcal{I} = 2000$ and $N_m = 1024$. The lines in (a) and (c) are the mean of α_{mean} over stochastic simulations with 100 randomly generated initial ansatz parameters for $p = 1$. The lines in (b) and (d) are the median of α_{min} . Shaded regions take percentiles 80% of data. These simulations use the mixing operator $\hat{M}_1(\beta)$ and the initial state $|\mathbf{w}\rangle_{mb}$ with $n = l = 4$. The final post-optimisation expectation value measurement shots of $N_M = 2^{16} = 65536$.

IV. SCALING RESULTS

To investigate the performance of our algorithm in solving the DGMVP model, we conduct stochastic simulations of models randomly selected from the financial market with varying asset numbers n and binary block lengths l . However, the stochastic noise in estimating the final expectation value $\langle C \rangle_{N_M}$ of the post-optimisation ansatz will increase with problem size if we fix the number of shots N_M . Thus, to gain a precise description of the optimised ansatz, we rebuild the parameterised quantum circuit using a statevector representation and calculate the exact expectation value $\langle C \rangle$. This allows us to benchmark the scaling of our quantum algorithm's performance with a range of metrics independent of N_M : the approximation ratios within the lower k percentile $\alpha_{\text{mean}}^{k\%}$ ($\alpha_{\text{mean}}^{100\%} = \alpha_{\text{mean}}$); the minimal value approximation ratio α_{min} ; the probability of measuring the minimal value P_{min} ; the probability of measuring global minimum P_{gm} among stochastic simulations. The results are presented in Figs. 9 to 11—for simulation details see Appx. J.

In Figs. 9 to 11, we compare classical methods to our quantum algorithm. We use the maxbias and the warm-started portfolio as both classical strategies and our initial states (see Sec. II B). For the warm-started portfolio, we post-select out the strategies that are the exact global minimum solutions in order to compare the level of improvement. For these two classical methods, we observe that the warm-started method outputs better results by orders of magnitude compared to the maxbias. For our quantum algorithm, we use DA as the optimiser and unfrozen-layerwise optimisation method with $\hat{M}_1(\beta)$. As the computational cost of optimising for the hyperparameters, N_m and \mathcal{I} , for all n and l configurations is high, we fix $N_m = 16$ and $\mathcal{I} = 2000$ as motivated by Appx. I. We justify fixing these values for all n and l as follows: Yanakiev *et al.* [51] demonstrates in appendix D that the number of shots required to estimate the approximation ratio to a fixed precision is independent of n and l . Further, we assume the number of optimisation steps to reach a given accuracy depends only on the number of parameters and hence the number of layers. Thus, we choose to fix the total number of shots used for optimisation for each layer.

In Fig. 9(a)(b), we observe our quantum algorithm achieves a significantly lower $\alpha_{\text{mean}}^{k\%}$ for all tested k and α_{min} compared to the maxbias method as a function of n and l . Additionally, we find $\alpha_{\text{mean}}^{k\%}$ and α_{min} improve with increasing p in the maxbias simulations. In particular, for the small l and n configurations, the post-optimised quantum circuit can measure the DGMVP solution with a relatively high probability—see Fig. 9(c)(d). We observe $\alpha_{\text{mean}}^{k\%}$ appears to saturate [see Fig. 9(a)(b)] and P_{min} decreases [see Fig. 9(e)(f)] as a function of n or l . This could

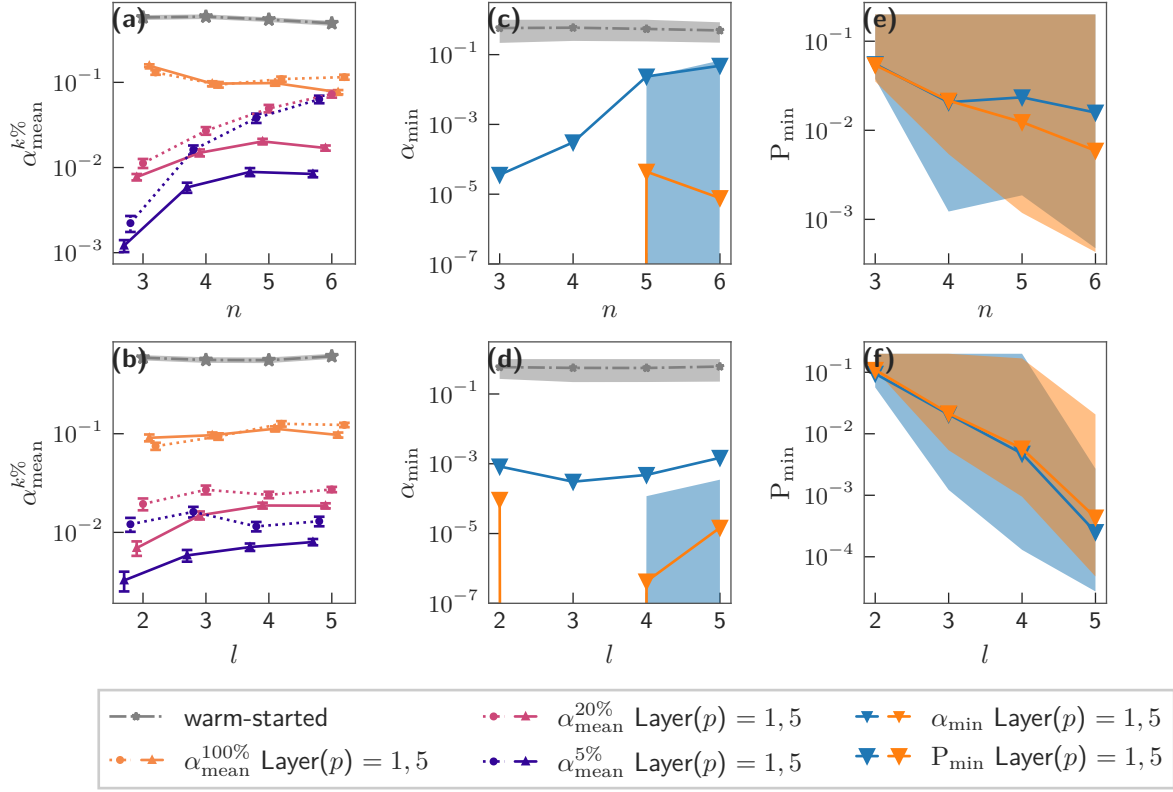


Figure 9. The $\alpha_{\text{mean}}^{k\%}$ (a)(b), α_{min} (c)(d) and P_{min} (e)(f) of the stochastic optimisation over 100 randomly generated DGMVP instances as a function of n with $l = 3$ (the top three panels) and l with $n = 4$ (the bottom three panels). The simulations use the initial state $|\mathbf{w}\rangle_{mb}$ and the mixing operator $\hat{M}_1(\beta)$, and the initial ansatz parameters are randomly generated. The grey lines are the approximation ratio of maxbias portfolios (also considered initial states). The coloured lines are the average data of $\alpha_{\text{mean}}^{k\%}$, α_{min} and P_{min} of the post-optimised ansatz. The shade regions and error bars in (a)(b) represent the standard error of the data. The shaded regions in (c)(d) are 25%-75% percentiles of the data, and the shaded regions in (e)(f) are 50%-100% percentiles of the data. The missing data points in (c)(d) for α_{min} correspond to values equal to 0. The classical optimiser is DA with $\mathcal{I} = 2000$ and $N_m = 16$, and the optimisation method is unfrozen-layerwise optimisation.

be because we use fixed values for N_m and \mathcal{I} for all the n and l configurations.

When using the warm-started initial state, we find $\alpha_{\text{mean}}^{100\%}$ is worse than the classical method (initial state) due to stochastic noise at finite N_m and \mathcal{I} during optimisation—see Fig. 10(a)(b). However, we find that while the optimisation increases the mean, it also skews the distribution towards the global minimum. Thus, the $\alpha_{\text{mean}}^{5\%}$ and $\alpha_{\text{mean}}^{20\%}$ curves lie close to the warm-started approximation ratio. Additionally, increasing p appears to increase $\alpha_{\text{mean}}^{k\%}$. This is likely due to an exacerbation of the stochastic noise from additional states being mixed into the statevector. The post-optimisation α_{min} for the warm-started initial state [see Fig. 10(c)(d)] is smaller than for the warm-started portfolio. The corresponding P_{min} [see Fig. 10(e)(f)] is almost constant as a function of n and l with fixed N_m and \mathcal{I} throughout the optimisation.

A global minimum is more important for investment because it represents the lowest-risk portfolio. Thus, in Fig. 11, we plot the inverse of the probability of measuring the global minimum $1/P_{gm}$. The number of measurements we require to find the true global minimum with some fixed success probability P_s is $N_M = \log(1 - P_s)/\log(1 - P_{gm})$. We benchmark this against the probability of measuring the global minimum when drawing uniformly random samples from both the constrained and unconstrained feasible region. The figure shows that the optimised quantum circuit has a significantly lower $1/P_{gm}$ than the constrained feasible region size, meaning the circuit can find the DGMVP solution with much higher probability for a single shot compared to a classical constrained random sampling method.

We also fit the inverse of the mean of P_{gm} (the crosses in Fig. 11) with the function $1/\bar{P}_{gm} = a \cdot B(n, l)^b$ where $B(n, l)$ is chosen as the constrained feasible region size (describe in Appx. B). We find $b = 0.76 \pm 0.30$ for the warm-started initial state, and $b = 0.51 \pm 0.09$ for the maxbias initial state—see Fig. 11(a). The ratio of the exponents of $1/\bar{P}_{gm}$ for the constrained classical sampling method to our quantum algorithm with warm-started and maxbias initial states are $1/0.76 \approx 1.32$ and $1/0.51 \approx 1.96$, respectively. This indicates our quantum algorithm has a more

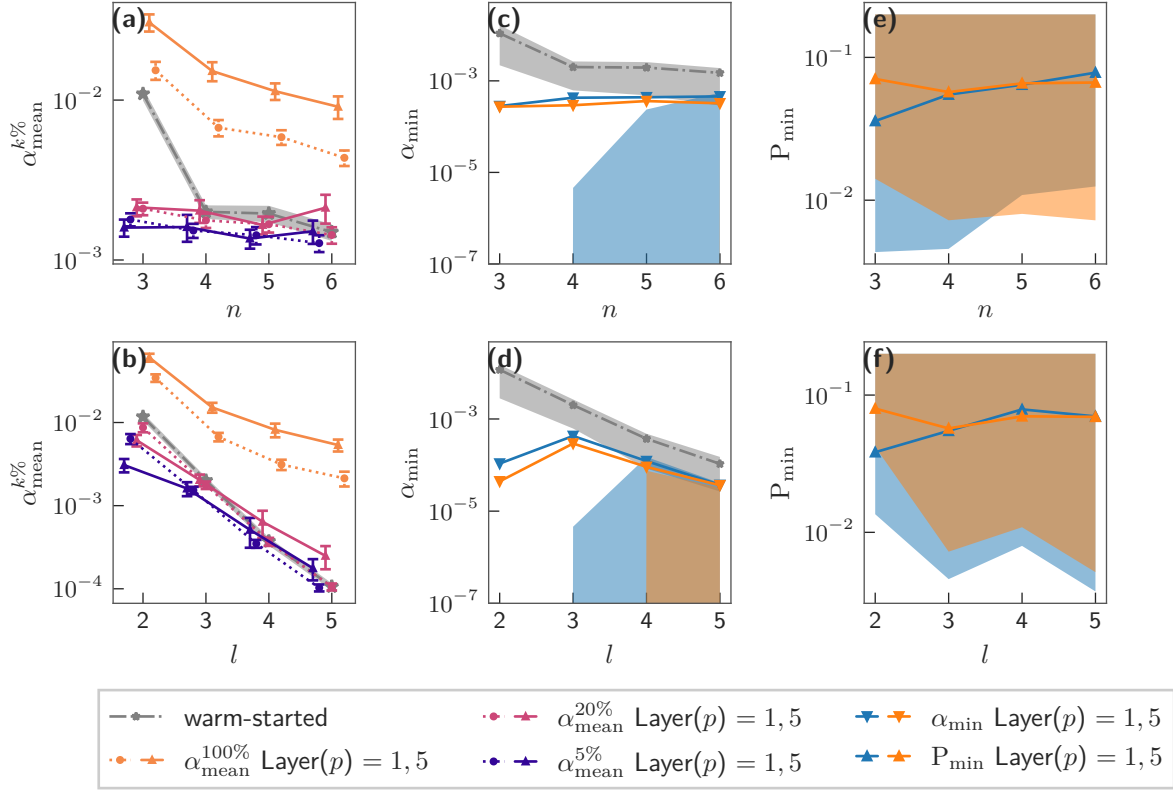


Figure 10. The $\alpha_{\text{mean}}^{k\%}$ (a)(b), α_{min} (c)(d) and P_{min} (e)(f) of the stochastic optimisation over 100 randomly generated DGMVP instances as a function of n with $l = 3$ (the top three panels) and l with $n = 4$ (the bottom three panels). The simulations use the initial state $|\mathbf{w}\rangle_{ws}$ and the mixing operator $\hat{M}_1(\beta)$, and the initial ansatz parameters are randomly generated. The grey lines are the approximation ratio of maxbias portfolios (also considered initial states). The coloured lines are the average data of $\alpha_{\text{mean}}^{k\%}$, α_{min} and P_{min} of the post-optimised ansatz. The shaded regions and error bars in (a)(b) represent the standard error of the data. The shaded regions in (c)(d) are 25%-75% percentiles of the data, and the shaded regions in (e)(f) are 50%-100% percentiles of the data. The classical optimiser is DA with $\mathcal{I} = 2000$ and $N_m = 16$, and the optimisation method is unfrozen-layerwise optimisation.

favourable power-law scaling with n . Similarly, we find $b = 0.66 \pm 0.01$ and $b = 1.11 \pm 0.05$ for the warm-started and maxbias initial states, respectively—see Fig. 11(b). Once again, we can consider the ratio of the exponents: $1/0.66 \approx 1.52$ and $1/1.11 \approx 0.90$ for the warm-started and maxbias initial states, respectively. Therefore, the scaling with l of our quantum algorithm appears to be more favourable than constrained classical sampling when using the warm-started initial state. The scalings in Fig. 11 indicate our quantum algorithm utilising the warm-started initial state may asymptotically obtain a reduction in the number of samples required to find the DGMVP solution over classical methods.

V. QUANTUM NOISE

This section compares the performance of our algorithm in the presence of thermal-relaxation noise with and without post-selection during optimisation. We utilise Qiskit’s thermal-relaxation noise model parameterised by an ensemble of T_1 and T_2 times drawn from normal distributions such that $T_2 \leq 2T_1$ with $T_1 \sim \mathcal{N}(50\mu s, 10\mu s)$ and $T_2 \sim \mathcal{N}(70\mu s, 10\mu s)$ [52]. To evaluate the influence of the quantum noise on our algorithm, we compare two methods: First, we use measurements on a simulated noisy quantum processor to estimate the expected value directly during the optimisation. Second, we use a post-selection method to enforce the constraint in Eq. (2a) when estimating the expectation value during the optimisation.

Noise-induced errors can invalidate the constraint in Eq. (2a), which will increase the difficulty of optimisation when we do not apply post-selection. However, even when we apply post-selection, optimisation will still be hampered by noise-induced errors that leave the constraint in Eq. (2a) satisfied. Further, the application of post-selection reduces

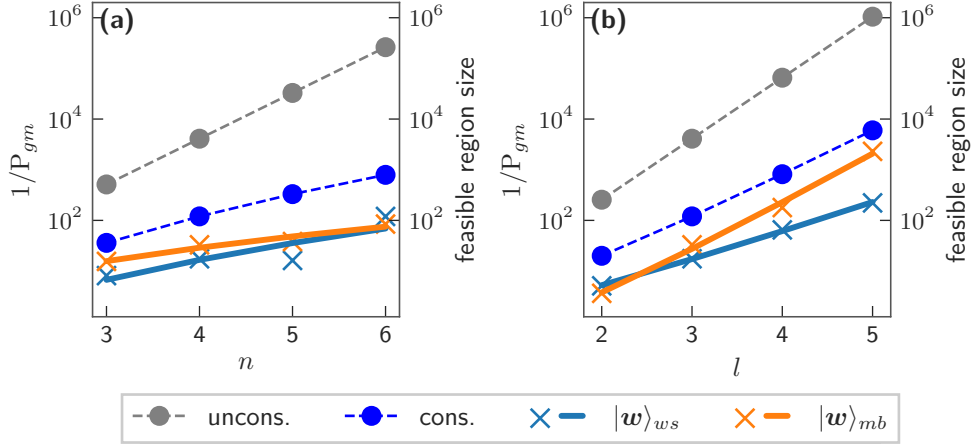


Figure 11. The inverse of the probability to measure the DGMVP solution ($1/P_{gm}$) and the feasible region scaling of the maxbias $|w\rangle_{mb}$ and warm-started $|w\rangle_{ws}$ initial states as a function of (a) n with $l = 3$, (b) l with $n = 4$. The maxbias optimisation data is the same as in Fig. 9, and the warm-started optimisation data is the same as in Fig. 10. In both panels, the left vertical axes are the $1/P_{gm}$ for the crosses and solid lines. Each cross is the average of the measured data, and the solid lines with the same colour fit the cross points with a function of $1/P_{gm} = a \cdot B(n, l)^b$ where $B(n, l)$ is the constraint feasible region size function. The right vertical axes denote the feasible region size as in Eq. (B5) for the grey (unconstraint feasible region) and the blue (constraint feasible region) dash line and round solid dots.

the number of shots that can be utilised for optimisation, which either increases the stochastic noise or the runtime. These effects compound to deteriorate the quality of the optimisation as shown in Fig. 12(a)(b). Finally, the average post-selection probability for both methods during the optimisation is presented in Fig. 12(c)(d), demonstrating roughly an order of magnitude increase in the number of shots required to maintain a fixed level of stochastic noise.

These results corroborate theoretical [53, 54] and numerical [40, 51, 55] results, suggesting only limited quantum advantage can be obtained by utilising variational quantum algorithms unless quantum noise levels are decreased by orders of magnitude. In a similar manner to stochastic noise, in Fig. 12(a), increasing measurement shots N_m can reduce the influence of quantum noise. In particular, the filtered method shows a small improvement in Fig. 12(a) compared to the unfiltered one as N_m is increased. However, when increasing p , the gap of α_{mean} closes and the probability of post-selection P_{ps} dropping sharply [see Fig. 12(b) and (d)].

VI. CONCLUSION

In this article, we have provided an end-to-end QAOA method to solve the DGMVP model. Further, we analysed the advantages and issues with the QAOA method for financial applications. Based on the DGMVP model, we designed the max-biased, ranked warm-started, approximated equal-weighted, and random-weighted initial states. The simulations show the max-biased and warm-started initial states outperform the others. We mapped the DGMVP model to a Hamiltonian C and designed corresponding cost operators $U(C, \gamma)$ with depth linear in the number of qubits. We designed a new hard mixing operator $\hat{M}_L(\beta)$ utilising two- and three-qubit excitations with efficient use of quantum gates using a phenomenon we call the quantum bridge. We numerically demonstrate that lower coupling distances between assets in the mixing operator makes the ansatz more readily optimisable.

Through comparative simulations, we found using DA with the limited number of expectation value access is better than one of the best local optimisation methods, COBYLA, even with large stochastic noise. We analyse two layerwise optimisation methods, frozen-layerwise, and unfrozen-layerwise, to improve the optimisability. Both methods outperform the fix ansatz optimisation approach, but unfrozen-layerwise indicates a better optimisation result in general.

In the scaling analysis section, we present our quantum algorithm's performance as a function of asset numbers n and block lengths l . On the one hand, we found our quantum algorithm can decrease the mean and minimal value approximation ratio from the maxbias initial state. On the other hand, the mean approximation ratio is not improved by optimisation from the warm-started initial state. However, the distribution is skewed towards the global minimum, which allows an improved solution to be measured with constant probability as a function of n and l . Moreover, further investigation shows that our quantum algorithm utilising the warm-started initial state may asymptotically (in n and

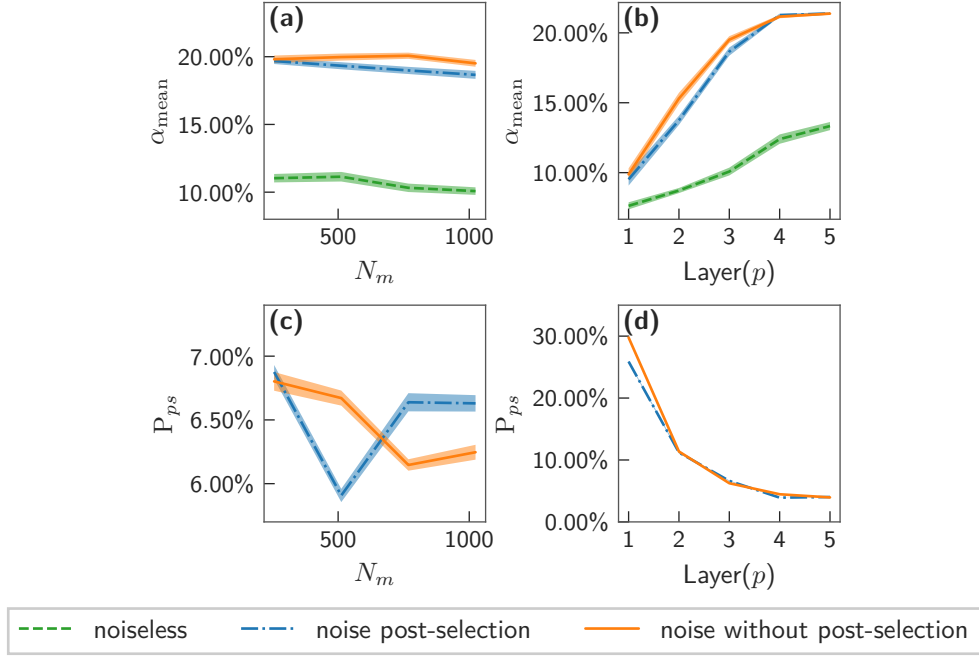


Figure 12. Performance of our QAOA in the presence of thermal relaxation noise with and without post-selection during the optimisation with optimiser COBYLA and optimisation method fix ansatz approach. We present both α_{mean} [(a) and (b)] and the average probability of post-selection during parameter optimisation P_{ps} [(c) and (d)] as functions of N_m with ansatz layer $p = 3$ [(a) and (c)] and layer p with $N_m = 1024$ [(b) and (d)]. The shaded regions in (a), (b), and (d) are the 25% to 75% quantile, and the shaded region in (c) is the 10% to 90% percentile of the data. These simulations use the mixing operator $\hat{M}_1(\beta)$ and the initial state $|\mathbf{w}\rangle_{mb}$ with $n = l = 4$. The final expectation value measurement shots $N_M = 2^{16} = 65536$. The results are a summarisation of over 100 simulations with random initial ansatz parameters.

l) outperform the classical method in the number of samples required to find the DGMVP solution.

Unfortunately, our quantum algorithm performs poorly in the presence of thermal relaxation noise. The impact can be mitigated by post-selecting out states not within the constrained feasible region. However, post-selection requires significantly more measurements to maintain a constant stochastic noise in the presence of quantum noise. This indicates drastic improvements in error rates or fault-tolerant quantum computation will be required for viable quantum finance applications.

In short, we showed that our quantum approximation algorithm allows us to predict the DGMVP. Our simulations and analyses reveal the potential advantages and disadvantages of implementing quantum algorithms in the financial industry in the future.

VII. ACKNOWLEDGEMENT

The authors thank Daniel Stilck França for valuable discussions on the DGMVP models and scaling figures. We thank Hanqing Wu and Binren Chen for the discussion of the binary encoding method, Jędrzej Burkat and Jonathan J. Thio for suggestions on mathematical notations, and David R. M. Arvidsson-Shukur and Normann Mertig for giving helpful suggestions and comments.

-
- [1] Michael A Nielsen and Isaac Chuang. *Quantum Computation and Quantum Information: 10th Anniversary Edition*. Cambridge University Press, Cambridge, 2010.
 - [2] Sam McArdle, Tyson Jones, Suguru Endo, Ying Li, Simon C. Benjamin, and Xiao Yuan. Variational ansatz-based quantum simulation of imaginary time evolution. *npj Quantum Information*, 5(1):75, September 2019.

- [3] M. Cerezo, Andrew Arrasmith, Ryan Babbush, Simon C. Benjamin, Suguru Endo, Keisuke Fujii, Jarrod R. McClean, Kosuke Mitarai, Xiao Yuan, Lukasz Cincio, and Patrick J. Coles. Variational quantum algorithms. *Nature Reviews Physics*, 3(9):625–644, September 2021.
- [4] Edward Farhi, Jeffrey Goldstone, and Sam Gutmann. A quantum approximate optimization algorithm, November 2014.
- [5] Stuart Hadfield, Zhihui Wang, Bryan O’gorman, Eleanor G Rieffel, Davide Venturelli, and Rupak Biswas. From the quantum approximate optimization algorithm to a quantum alternating operator ansatz. *Algorithms*, 12(2):34, February 2019.
- [6] Daniel J. Egger, Jakub Marecek, and Stefan Woerner. Warm-starting quantum optimization. *Quantum*, 5:479, June 2021.
- [7] Sergey Bravyi, Alexander Kliesch, Robert Koenig, and Eugene Tang. Hybrid quantum-classical algorithms for approximate graph coloring. *Quantum*, 6:678, March 2022.
- [8] Edward Farhi, Jeffrey Goldstone, Sam Gutmann, and Leo Zhou. The Quantum Approximate Optimization Algorithm and the Sherrington-Kirkpatrick Model at Infinite Size. *Quantum*, 6:759, July 2022.
- [9] Samuel Fernández-Lorenzo, Diego Porras, and Juan José García-Ripoll. Hybrid quantum-classical optimization with cardinality constraints and applications to finance. *Quantum Science and Technology*, 6(3):034010, June 2021.
- [10] Alberto Peruzzo, Jarrod McClean, Peter Shadbolt, Man Hong Yung, Xiao Qi Zhou, Peter J. Love, Alán Aspuru-Guzik, and Jeremy L. O’Brien. A variational eigenvalue solver on a photonic quantum processor. *Nature Communications*, 5(1):4213, 2014.
- [11] Nicholas Slate, Edric Matwiejew, Samuel Marsh, and JB Wang. Quantum walk-based portfolio optimisation. *Quantum*, 5:513, July 2021.
- [12] Fernando G. S. L. Brandão, Richard Kueng, and Daniel Stilck França. Faster quantum and classical SDP approximations for quadratic binary optimization. *Quantum*, 6:625, January 2022.
- [13] Patrick Rebertost and Seth Lloyd. Quantum computational finance: Quantum algorithm for portfolio optimization. *KI - Künstliche Intelligenz*, August 2024.
- [14] Mark Hodson, Brendan Ruck, Hugh Ong, David Garvin, and Stefan Dulman. Portfolio rebalancing experiments using the quantum alternating operator ansatz, November 2019.
- [15] Sebastian Brandhofer, Daniel Braun, Vanessa Dehn, Gerhard Hellstern, Matthias Hüls, Yanjun Ji, Ilia Polian, Amandeep Singh Bhatia, and Thomas Wellens. Benchmarking the performance of portfolio optimization with QAOA. *Quantum Information Processing*, 22(1):25, December 2022.
- [16] Dylan Herman, Cody Googin, Xiaoyuan Liu, Alexey Galda, Ilya Safro, Yue Sun, Marco Pistoia, and Yuri Alexeev. A survey of quantum computing for finance, January 2022.
- [17] Bingren Chen, Hanqing Wu, Haomu Yuan, Lei Wu, and Xin Li. Quasi-binary encoding based quantum alternating operator ansatz, January 2024.
- [18] Leo Zhou, Sheng-Tao Wang, Soonwon Choi, Hannes Pichler, and Mikhail D. Lukin. Quantum approximate optimization algorithm: Performance, mechanism, and implementation on near-term devices. *Physical Review X*, 10(2):021067, June 2020.
- [19] Harry Markowitz. Portfolio selection. *The Journal of Finance*, 7:77–91, March 1952.
- [20] Petter N Kolm, Reha Tütüncü, and Frank J Fabozzi. 60 years of portfolio optimization: Practical challenges and current trends. *European Journal of Operational Research*, 234(2):356–371, April 2014.
- [21] Eric Jondeau and Michael Rockinger. Optimal portfolio allocation under higher moments. *European Financial Management*, 12(1):29–55, January 2006.
- [22] Robert A Haugen. *The New Finance: The Case against Efficient Markets*. Prentice Hall, 1994.
- [23] Roger G Clarke, Harindra De Silva, and Steven Thorley. Minimum-variance portfolios in the u.s. equity market. *The journal of portfolio management*, 33(1):10–24, 2006.
- [24] Roger Clarke, Harindra De Silva, and Steven Thorley. Minimum-variance portfolio composition. *Journal of Portfolio Management*, 37(2):31, 2011.
- [25] Louis K. C. Chan, Jason Karceski, and Josef Lakonishok. On portfolio optimization: Forecasting covariances and choosing the risk model. *The Review of Financial Studies*, 12(5):937–974, June 2015.
- [26] Google AI Quantum, Collaborators*†, Frank Arute, Kunal Arya, Ryan Babbush, Dave Bacon, Joseph C. Bardin, Rami Barends, Sergio Boixo, Michael Broughton, Bob B. Buckley, David A. Buell, Brian Burkett, Nicholas Bushnell, Yu Chen, Zijun Chen, Benjamin Chiaro, Roberto Collins, William Courtney, Sean Demura, Andrew Dunsworth, Edward Farhi, Austin Fowler, Brooks Foxen, Craig Gidney, Marissa Giustina, Rob Graff, Steve Habegger, Matthew P. Harrigan, Alan Ho, Sabrina Hong, Trent Huang, William J. Huggins, Lev Ioffe, Sergei V. Isakov, Evan Jeffrey, Zhang Jiang, Cody Jones, Dvir Kafri, Kostyantyn Kechedzhi, Julian Kelly, Seon Kim, Paul V. Klimov, Alexander Korotkov, Fedor Kostritsa, David Landhuis, Pavel Laptev, Mike Lindmark, Erik Lucero, Orion Martin, John M. Martinis, Jarrod R. McClean, Matt McEwen, Anthony Megrant, Xiao Mi, Masoud Mohseni, Wojciech Mruczkiewicz, Josh Mutus, Ofer Naaman, Matthew Neeley, Charles Neill, Hartmut Neven, Murphy Yuezhen Niu, Thomas E. O’Brien, Eric Ostby, Andre Petukhov, Harald Putterman, Chris Quintana, Pedram Roushan, Nicholas C. Rubin, Daniel Sank, Kevin J. Satzinger, Vadim Smelyanskiy, Doug Strain, Kevin J. Sung, Marco Szalay, Tyler Y. Takeshita, Amit Vainsencher, Theodore White, Nathan Wiebe, Z. Jamie Yao, Ping Yeh, and Adam Zalcman. Hartree-fock on a superconducting qubit quantum computer. *Science*, 369(6507):1084–1089, August 2020.
- [27] Harper R. Grimsley, George S. Barron, Edwin Barnes, Sophia E. Economou, and Nicholas J. Mayhall. Adaptive, problem-tailored variational quantum eigensolver mitigates rough parameter landscapes and barren plateaus. *npj Quantum Information*, 9(1):19, March 2023.

- [28] Jeremy Cook, Stephan Eidenbenz, and Andreas Bärttschi. The quantum alternating operator ansatz on maximum k-vertex cover. In *2020 IEEE International Conference on Quantum Computing and Engineering (QCE)*, pages 83–92. IEEE, 2020.
- [29] Reuben Tate, Jai Moondra, Bryan Gard, Greg Mohler, and Swati Gupta. Warm-started QAOA with Custom Mixers Provably Converges and Computationally Beats Goemans-Williamson’s Max-Cut at Low Circuit Depths. *Quantum*, 7:1121, September 2023.
- [30] Zhihui Wang, Nicholas C. Rubin, Jason M. Dominy, and Eleanor G. Rieffel. xy mixers: Analytical and numerical results for the quantum alternating operator ansatz. *Physical Review A*, 101(1):012320, January 2020.
- [31] Andreas Bärttschi and Stephan Eidenbenz. Grover mixers for qaoa: Shifting complexity from mixer design to state preparation. In *2020 IEEE International Conference on Quantum Computing and Engineering (QCE)*, pages 72–82. IEEE, 2020.
- [32] Panagiotis KI Barkoutsos, Giacomo Nannicini, Anton Robert, Ivano Tavernelli, and Stefan Woerner. Improving variational quantum optimization using cvar. *Quantum*, 4:256, April 2020.
- [33] Dan-Bo Zhang, Bin-Lin Chen, Zhan-Hao Yuan, and Tao Yin. Variational quantum eigensolvers by variance minimization. *Chinese Physics B*, 31(12):120301, 2022.
- [34] David Wierichs, Christian Gogolin, and Michael Kastoryano. Avoiding local minima in variational quantum eigensolvers with the natural gradient optimizer. *Physics Review Research*, 2:043246, November 2020.
- [35] Michael Streif and Martin Leib. Training the quantum approximate optimization algorithm without access to a quantum processing unit. *Quantum Science and Technology*, 5(3):034008, May 2020.
- [36] Mario Fernández-Pendás, Elías F Combarro, Sofia Vallecorsa, José Ranilla, and Ignacio F Rúa. A study of the performance of classical minimizers in the quantum approximate optimization algorithm. *Journal of Computational and Applied Mathematics*, 404:113388, 2022.
- [37] Aidan Pellow-Jarman, Shane McFarthing, Ilya Sinayskiy, Daniel K. Park, Anban Pillay, and Francesco Petruccione. The effect of classical optimizers and ansatz depth on qaoa performance in noisy devices. *Scientific Reports*, 14(1):16011, July 2024.
- [38] Nicholas Chancellor. Domain wall encoding of discrete variables for quantum annealing and qaoa. *Quantum Science and Technology*, 4(4):045004, August 2019.
- [39] Panagiotis G. Anastasiou, Yanzhu Chen, Nicholas J. Mayhall, Edwin Barnes, and Sophia E. Economou. Tetris-adapt-vqe: An adaptive algorithm that yields shallower, denser circuit ansätze. *Physical Review Research*, 6(1):013254, March 2024.
- [40] Christopher K. Long, Kieran Dalton, Crispin H. W. Barnes, David R. M. Arvidsson-Shukur, and Normann Mertig. Layering and subpool exploration for adaptive variational quantum eigensolvers: Reducing circuit depth, runtime, and susceptibility to noise. *Physical Review A*, 109:042413, Apr 2024.
- [41] Yordan S. Yordanov, David R. M. Arvidsson-Shukur, and Crispin H. W. Barnes. Efficient quantum circuits for quantum computational chemistry. *Physical Review A*, 102(6):062612, December 2020.
- [42] M. J. D. Powell. *A Direct Search Optimization Method That Models the Objective and Constraint Functions by Linear Interpolation*, pages 51–67. Springer Netherlands, Dordrecht, 1994.
- [43] Yang Xiang, DY Sun, W Fan, and XG Gong. Generalized simulated annealing algorithm and its application to the thomson model. *Physics Letters A*, 233(3):216–220, 1997.
- [44] Aidan Pellow-Jarman, Ilya Sinayskiy, Anban Pillay, and Francesco Petruccione. A comparison of various classical optimizers for a variational quantum linear solver. *Quantum Information Processing*, 20(6):202, June 2021.
- [45] Wim Lavrijsen, Ana Tudor, Juliane Müller, Costin Iancu, and Wibe de Jong. Classical optimizers for noisy intermediate-scale quantum devices. In *2020 IEEE International Conference on Quantum Computing and Engineering (QCE)*, pages 267–277, 2020.
- [46] Pranav Gokhale, Olivia Angiuli, Yongshan Ding, Kaiwen Gui, Teague Tomesh, Martin Suchara, Margaret Martonosi, and Frederic T. Chong. $o(n^3)$ measurement cost for variational quantum eigensolver on molecular hamiltonians. *IEEE Transactions on Quantum Engineering*, 1:1–24, 2020.
- [47] Andrea Skolik, Jarrod R. McClean, Masoud Mohseni, Patrick van der Smagt, and Martin Leib. Layerwise learning for quantum neural networks. *Quantum Machine Intelligence*, 3(1):5, January 2021.
- [48] Linghua Zhu, Ho Lun Tang, George S. Barron, F. A. Calderon-Vargas, Nicholas J. Mayhall, Edwin Barnes, and Sophia E. Economou. Adaptive quantum approximate optimization algorithm for solving combinatorial problems on a quantum computer. *Physics Review Research*, 4:033029, July 2022.
- [49] E. Campos, D. Rabinovich, V. Akshay, and J. Biamonte. Training saturation in layerwise quantum approximate optimization. *Physical Review A*, 104:L030401, September 2021.
- [50] Xinwei Lee, Xinjian Yan, Ningyi Xie, Dongsheng Cai, Yoshiyuki Saito, and Nobuyoshi Asai. Iterative layerwise training for the quantum approximate optimization algorithm. *Physical Review A*, 109:052406, May 2024.
- [51] Nikola Yanakiev, Normann Mertig, Christopher K. Long, and David R. M. Arvidsson-Shukur. Dynamic adaptive quantum approximate optimization algorithm for shallow, noise-resilient circuits. *Physical Review A*, 109:032420, March 2024.
- [52] Ali Javadi-Abhari, Matthew Treinish, Kevin Krsulich, Christopher J. Wood, Jake Lishman, Julien Gacon, Simon Martiel, Paul D. Nation, Lev S. Bishop, Andrew W. Cross, Blake R. Johnson, and Jay M. Gambetta. Quantum computing with Qiskit, 2024.
- [53] Daniel Stilck França and Raul García-Patrón. Limitations of optimization algorithms on noisy quantum devices. *Nature Physics*, 17(11):1221–1227, November 2021.
- [54] Giacomo De Palma, Milad Marvian, Cambyse Rouzé, and Daniel Stilck França. Limitations of variational quantum algorithms: A quantum optimal transport approach. *PRX Quantum*, 4:010309, January 2023.

- [55] Kieran Dalton, Christopher K. Long, Yordan S. Yordanov, Charles G. Smith, Crispin H. W. Barnes, Normann Mertig, and David R. M. Arvidsson-Shukur. Quantifying the effect of gate errors on variational quantum eigensolvers for quantum chemistry. *npj Quantum Information*, 10(1), January 2024.
- [56] Rama Malladi and Frank Fabozzi. Equal-weighted strategy: Why it outperforms value-weighted strategies? theory and evidence. *Journal of Asset Management*, 18:188–208, May 2017.

Appendix A: Covariance matrix for portfolio optimisation

A financial asset i has typically a time series of price data. If we represent it by a random variable $P_i(\mathbf{T})$, where $\mathbf{T} = (T_1, T_2, \dots, T_n)$ is the time series, a σ_{ij} can be calculated as

$$\sigma_{ij} = \text{cov}(P_i(\mathbf{T}), P_j(\mathbf{T})) \quad (\text{A1})$$

where cov is the covariance. This article generates a portfolio basket among 32 stocks from the NASDAQ and NYSE from "2023-03-01" to "2023-06-30". The price data uses their daily adjust-close price over the same 100 days as raw data. An example of a basket of 8 selected stocks covariance matrix is shown in Fig. 13.

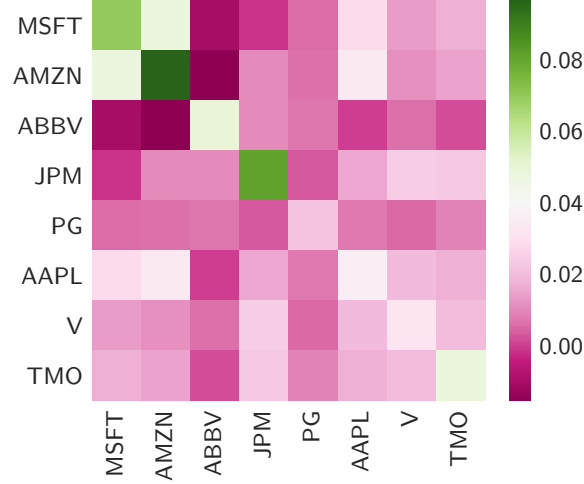


Figure 13. The covariance matrix of 8 selected stocks. MSFT means Microsoft Corp, AMZN means Amazon.com Inc, ABBV means AbbVie Inc, JPM means JPMorgan Chase & Co, PG means Procter & Gamble Co, AAPL means Apple Inc, V means Visa Inc, and TMO means Thermo Fisher Scientific Inc.

Appendix B: Feasible region size of the DGMVP with and without the budget constraint

This appendix reveals the method to calculate the feasible region size of the DGMVP with and without the budget constraint, which also represents the total number of portfolio strategies. The feasible region size for the DGMVP [Eq. (1)] without the constraint is 2^{ln} , where l is the number of binary variables for encoding each asset and n is the number of assets.

For the constrained DGMVP as in Eq. (1), the total number of portfolio strategies can be calculated inductively. Let $A(n, N)$ be the number of strategies on n assets with N trading lots. Suppose we spend m trading lots on the n th asset then we will have $A(n-1, N-m)$ remaining strategies on the remaining $n-1$ assets. Therefore, the total number of strategies will be:

$$A(n, N) = A(n-1, N) + A(n-1, N-1) + \dots + A(n-1, 1) + A(n-1, 0) \quad (\text{B1})$$

Inductively, $A(n, N)$ can be calculated as proven in Lemma 1.

Lemma 1. *The number of strategies $A(n, N)$ of n assets with N trading lots is*

$$A(n, N) = \binom{N+n-1}{n-1}. \quad (\text{B2})$$

Proof. Suppose Eq. (B2) holds true for some specific n and all N' , then

$$\begin{aligned} A(n+1, N') &= \sum_{m=0}^{N'} A(n, m) \\ &= \sum_{m=0}^{N'} \binom{m+n-1}{n-1} \\ &= \binom{N'+n+1-1}{n+1-1}, \end{aligned} \quad (\text{B3})$$

where the last equality follows from the rules of Pascal's triangle:

$$\binom{j}{k} \equiv \binom{j+1}{k+1} - \binom{j}{k+1}. \quad (\text{B4})$$

Note that $A(1, N') = 1 \equiv \binom{N'}{0}$ for all N' . Thus, by induction Eq. (B2) must hold for all n and N' . \square

When considering a binary encoding, we define a new notation of the number of strategies:

$$B(n, l) = \binom{2^l + n - 2}{n - 1}, \quad (\text{B5})$$

where l is the binary block length for encoding each asset.

In Fig. 11, we observe both the constrained and unconstrained feasible reason sizes grow exponentially. However, the size of the feasible region with the budget constraint grows much slower than the one without constraint. The gaps become more significant on an exponential scale, which indicates our hard mixing operator will exclude drastic amounts of unqualified solutions in a larger n, l configuration.

Appendix C: Initial state extra preparation methods and simulations

In this appendix, we compare the initial states defined in Sec. IIB and below. To facilitate this comparison, we present both α_{mean} and α_{min} as a function of p for each initial state in Fig. 14. We find distinctly different trends in α_{mean} and α_{min} : On the one hand for α_{mean} , there is an optimal p before which the stochastic measurement noise causes the optimiser to return increasingly poor values for α_{mean} —for a thorough analysis of stochastic measurement noise see Sec. IIIA. On the other hand α_{min} generally decreases with increasing p and is impacted less by the stochastic measurement noise. Fortunately, despite optimising with respect to estimated averaged values, it is α_{min} that defines the quality of our final solution to the DGMVP model. Thus, we conclude that $|\mathbf{w}\rangle_{ws}$ performs the best followed by $|\mathbf{w}\rangle_{mb}$. Henceforth, we will restrict our investigations to $|\mathbf{w}\rangle_{ws}$ and $|\mathbf{w}\rangle_{mb}$; not only for their superior performance but also as they represent two disjoint areas for potential quantum advantage: $|\mathbf{w}\rangle_{ws}$ represents a *prior-knowledge* initialisation as a good classical approximation obtainable in polynomial time and allows us to probe the potential for improved quantum-enabled approximations in the non-asymptotic regime. Alternatively, $|\mathbf{w}\rangle_{mb}$ represents a *zero-knowledge* initialisation allowing us to investigate possible quantum-enabled accelerations in obtaining an approximation at least as good as $|\mathbf{w}\rangle_{ws}$.

The approximated equal-weighted state $|\mathbf{w}\rangle_{ew}$:—This state represents an approximation to an equal-weighted portfolio strategy (50/50 portfolio strategy) and consists of buying each asset in equal weight w.r.t. the total capital. Researchers often use an equal-weighted portfolio strategy as a benchmark for other strategies [56]. An approximated equal-weighted strategy of the DGMVP can be found by iteratively buying the unit trading lot (binary precision a) from the first asset to the end. For a loop of buying one trading lot for n assets, the total spent is na . The maximal repetition of completing this buying loop is at most $\lfloor 1/(na) \rfloor$ times because of the budget constraint. Then, we assign remaining budgets to buy one trading lot a sequentially from the first asset to the p th until no money left and get an equation as

$$1 - \left\lfloor \frac{1}{na} \right\rfloor na - pa = 0. \quad (\text{C1})$$

An approximated equal-weighted state $|\mathbf{w}\rangle_{ew}$ is to prepare the asset weights as

$$w_i = \begin{cases} a\hat{z} + a, & i \leq p \\ a\hat{z}, & i > p \end{cases}, \quad (\text{C2})$$

where $\hat{z} = \lfloor 1/(na) \rfloor$.

The random-weighted state $|\mathbf{w}\rangle_{rd}$:— This state is prepared by generating a uniformly random set of weights satisfying the budget constraint and the binary block encoding.

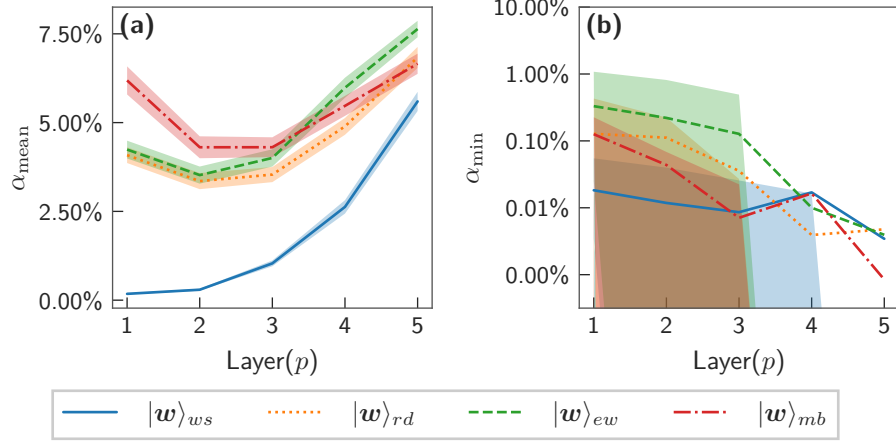


Figure 14. A comparison of the impact of initial states on the performance of our QAOA ansatz: (a) α_{mean} , (b) α_{min} . We present the optimised α_{mean} and corresponding α_{min} over randomly selected GMVP instances from the market as a function of the number of the layer p . We compare the warm-started $|\mathbf{w}\rangle_{ws}$, randomly initialised $|\mathbf{w}\rangle_{rd}$, the equally weighted $|\mathbf{w}\rangle_{ew}$, and the maxbias $|\mathbf{w}\rangle_{mb}$ initial states. The shaded region in (a) indicates the standard error of the data, and the shaded region in (b) indicates the 50% to 90% percentile of data. We only use warm-started states that are not already equal to the global minimum to facilitate a fair comparison. The QAOA ansatz uses the mixing operator $\hat{M}_1(\beta)$ with the ansatz initial parameters randomly generated. The optimiser is DA, and the optimisation method is the fix ansatz approach with the number of shots during optimisation $N_m = 2^4 = 16$ and the final expectation value measurement shots $N_M = 2^{16} = 65536$.

Appendix D: Quantum bridge on two-qubit excitations

In this appendix, we analyse the action of two-qubit excitations in a specific design pattern. We define the following pair of operator to exchange qubit excitation between two qubits:

$$\begin{aligned} S_{AB}^- &:= Q_A^\dagger Q_B - Q_A Q_B^\dagger \\ S_{AB}^+ &:= Q_A^\dagger Q_B + Q_A Q_B^\dagger, \end{aligned} \quad (\text{D1})$$

where A and B are the qubits sub-systems acted upon non-trivially. By expanding them with Pauli operators, we have

$$S_{AB}^+ = \frac{1}{2}(X_A X_B + Y_A Y_B) \quad (\text{D2})$$

$$S_{AB}^- = \frac{i}{2}(X_A Y_B - Y_A X_B). \quad (\text{D3})$$

If we apply a Pauli-Z operator to one of the qubit sub-systems of S_{AB}^\pm , we have,

$$\begin{aligned} S_{AB}^- Z_A &= -S_{AB}^- Z_B = \frac{i}{2}(X_A Y_B - Y_A X_B) Z_A = \frac{1}{2}(X_A X_B + Y_A Y_B) = S_{AB}^+, \\ S_{AB}^+ Z_A &= S_{AB}^+ Z_B = \frac{1}{2}(X_A X_B + Y_A Y_B) Z_A = \frac{1}{2}(-i Y_A X_B + i X_A Y_B) = \frac{i}{2}(X_A Y_B - Y_A X_B) = S_{AB}^-, \\ Z_A S_{AB}^- &= -Z_B S_{AB}^- = -S_{AB}^- Z_A = -S_{AB}^+, \\ Z_A S_{AB}^+ &= Z_B S_{AB}^+ = -S_{AB}^+ Z_A = S_{AB}^-. \end{aligned} \quad (\text{D4})$$

If we apply $Z_A Z_B$, then,

$$\begin{aligned} S_{AB}^- Z_A Z_B &= Z_A Z_B S_{AB}^- = \frac{i}{2} (X_A Y_B - Y_A X_B) Z_A Z_B = \frac{i}{2} (Y_A X_B - X_A Y_B) = -S_{AB}^- \\ S_{AB}^+ Z_A Z_B &= Z_A Z_B S_{AB}^+ = \frac{1}{2} (X_A X_B + Y_A Y_B) Z_A Z_B = -S_{AB}^+. \end{aligned} \quad (\text{D5})$$

We can expand the exponential of S_{AB}^- as

$$\begin{aligned} e^{\beta S_{AB}^-} &= e^{\frac{i\beta}{2} (X_A Y_B - Y_A X_B)} = e^{\frac{i\beta}{2} X_A Y_B} e^{-\frac{i\beta}{2} Y_A X_B} \\ &= (\cos \frac{\beta}{2} \mathbb{1} + i \sin \frac{\beta}{2} X_A Y_B) (\cos \frac{\beta}{2} \mathbb{1} - i \sin \frac{\beta}{2} Y_A X_B) \\ &= \cos^2 \frac{\beta}{2} \mathbb{1} + \sin^2 \frac{\beta}{2} Z_A Z_B + i \sin \frac{\beta}{2} \cos \frac{\beta}{2} X_A Y_B - i \sin \frac{\beta}{2} \cos \frac{\beta}{2} Y_A X_B \\ &= \cos^2 \frac{\beta}{2} \mathbb{1} + \sin^2 \frac{\beta}{2} Z_A Z_B + i \frac{\sin \beta}{2} (X_A Y_B - Y_A X_B) \\ &= \cos^2 \frac{\beta}{2} \mathbb{1} + \sin^2 \frac{\beta}{2} Z_A Z_B + \sin \beta S_{AB}^- \end{aligned} \quad (\text{D6})$$

where $\mathbb{1}$ and $Z_A Z_B$ leave the occupations of the computational basis states invariant, S_{AB}^- varies the occupations, and the parameter β controls the magnitude of the change.

If we apply another operator $e^{\beta S_{BC}^-}$ to the right side of $e^{\beta S_{AB}^-}$ [see Fig. 15(a)], we have

$$\begin{aligned} &e^{\beta S_{AB}^-} e^{\beta S_{BC}^-} \\ &= e^{\frac{i\beta}{2} (X_A Y_B - Y_A X_B)} e^{\frac{i\beta}{2} (X_B Y_C - Y_B X_C)} \\ &= \left(\cos^2 \left(\frac{\beta}{2} \right) \mathbb{1} + \sin^2 \left(\frac{\beta}{2} \right) Z_A Z_B + \sin(\beta) S_{AB}^- \right) \left(\cos^2 \left(\frac{\beta}{2} \right) \mathbb{1} + \sin^2 \left(\frac{\beta}{2} \right) Z_B Z_C + \sin(\beta) S_{BC}^- \right) \\ &= \cos^4 \left(\frac{\beta}{2} \right) \mathbb{1} + \frac{1}{4} \sin^2(\beta) Z_B Z_C + \frac{1}{4} \sin^2(\beta) Z_A Z_B + \sin^4 \left(\frac{\beta}{2} \right) Z_A Z_C + \sin(\beta) \cos^2 \left(\frac{\beta}{2} \right) S_{BC}^- + \sin(\beta) \cos^2 \left(\frac{\beta}{2} \right) S_{AB}^- \\ &\quad - \sin^2 \left(\frac{\beta}{2} \right) \sin(\beta) Z_A S_{BC}^+ - \sin^2 \left(\frac{\beta}{2} \right) \sin(\beta) S_{AB}^+ Z_C + \sin^2(\beta) S_{AB}^- S_{BC}^-. \end{aligned} \quad (\text{D7})$$

If we continue to add another operator $e^{\beta S_{BC}^-}$ to the left of $e^{\beta S_{AB}^-}$ [see Fig. 15(b)], we have

$$\begin{aligned}
& e^{\beta S_{BC}^-} e^{\beta S_{AB}^-} e^{\beta S_{BC}^-} \\
&= \left(e^{\beta S_{BC}^-} e^{\beta S_{AB}^-} \right) e^{\beta S_{BC}^-} \\
&= \cos^6 \left(\frac{\beta}{2} \right) \mathbb{1} + \frac{1}{4} \cos^2 \left(\frac{\beta}{2} \right) \sin^2(\beta) Z_A Z_B + \sin(\beta) \cos^4 \left(\frac{\beta}{2} \right) S_{AB}^- \\
&\quad + \frac{1}{4} \sin^2(\beta) \cos^2 \left(\frac{\beta}{2} \right) Z_B Z_C + \frac{1}{4} \sin^2(\beta) \sin^2 \left(\frac{\beta}{2} \right) Z_A Z_C + \frac{1}{4} \sin^3(\beta) Z_C S_{AB}^+ \\
&\quad + \frac{1}{4} \sin^2(\beta) \cos^2 \left(\frac{\beta}{2} \right) Z_A Z_B + \frac{1}{4} \sin^2(\beta) \sin^2 \left(\frac{\beta}{2} \right) \mathbb{1} - \frac{1}{4} \sin^3 \beta S_{AB}^- \\
&\quad + \sin^4 \left(\frac{\beta}{2} \right) \cos^2 \left(\frac{\beta}{2} \right) Z_A Z_C + \sin^6 \left(\frac{\beta}{2} \right) Z_B Z_C - \sin^4 \left(\frac{\beta}{2} \right) \sin(\beta) Z_C S_{AB}^+ \\
&\quad + \sin(\beta) \cos^4 \left(\frac{\beta}{2} \right) S_{BC}^- + \frac{1}{4} \sin^3(\beta) S_{BC}^+ Z_A + \sin^2(\beta) \cos^2 \left(\frac{\beta}{2} \right) S_{BC}^- S_{AB}^- \\
&\quad + \sin(\beta) \cos^4 \left(\frac{\beta}{2} \right) S_{AB}^- - \frac{1}{4} \sin^3(\beta) S_{AB}^- + \sin^2(\beta) \cos^2 \left(\frac{\beta}{2} \right) S_{AB}^- S_{AB}^- \\
&\quad - \frac{1}{4} \sin^3(\beta) Z_A S_{BC}^+ + \sin^4 \left(\frac{\beta}{2} \right) \sin(\beta) S_{BC}^- + \sin^2 \left(\frac{\beta}{2} \right) \sin^2(\beta) S_{BC}^+ S_{AB}^+ \\
&\quad - \frac{1}{4} \sin^3(\beta) S_{AB}^+ Z_C + \sin^4 \left(\frac{\beta}{2} \right) \sin(\beta) S_{AB}^+ Z_C - \sin^2 \left(\frac{\beta}{2} \right) \sin^2(\beta) S_{AB}^+ S_{AB}^- Z_C \\
&\quad + \sin^2(\beta) \cos^2 \left(\frac{\beta}{2} \right) S_{AB}^- S_{BC}^- + \sin^2(\beta) \sin^2 \left(\frac{\beta}{2} \right) S_{AB}^- S_{BC}^- Z_A Z_B \\
&= \left(\cos^6 \frac{\beta}{2} + \frac{1}{4} \sin^2 \beta \sin^2 \frac{\beta}{2} \right) \mathbb{1} + \frac{1}{2} \cos^2 \frac{\beta}{2} \sin^2 \beta Z_A Z_B \\
&\quad + \frac{1}{2} \sin^2(\beta) \sin^2 \left(\frac{\beta}{2} \right) Z_A Z_C + \left(\frac{1}{4} \sin^2(\beta) \cos^2 \left(\frac{\beta}{2} \right) + \sin^6 \left(\frac{\beta}{2} \right) \right) Z_B Z_C \\
&\quad + \left(2 \sin(\beta) \cos^4 \left(\frac{\beta}{2} \right) - \frac{1}{2} \sin^3(\beta) \right) S_{AB}^- + \left(\sin(\beta) \cos^4 \left(\frac{\beta}{2} \right) + \sin^4 \left(\frac{\beta}{2} \right) \sin(\beta) \right) S_{BC}^- \\
&\quad + \sin^2(\beta) \cos^2 \left(\frac{\beta}{2} \right) S_{AB}^- S_{AB}^- - \sin^2 \left(\frac{\beta}{2} \right) \sin^2(\beta) S_{AB}^+ S_{AB}^- Z_C + \sin^2(\beta) \cos^2 \left(\frac{\beta}{2} \right) S_{BC}^- S_{AB}^- \\
&\quad + \sin^2 \left(\frac{\beta}{2} \right) \sin^2(\beta) S_{BC}^+ S_{AB}^+ + \sin^2(\beta) \cos^2 \left(\frac{\beta}{2} \right) S_{AB}^- S_{BC}^- + \sin^2(\beta) \sin^2 \left(\frac{\beta}{2} \right) S_{AB}^- S_{BC}^- Z_A Z_B \\
&= k_1^\beta \mathbb{1} + k_2^\beta Z_A Z_B + k_3^\beta Z_B Z_C + k_4^\beta S_{AB}^- + k_5^\beta S_{BC}^- + k_6^\beta S_{AC}^+,
\end{aligned} \tag{D8}$$

where

$$\begin{aligned}
k_1^\beta &= \cos^6 \frac{\beta}{2} + \frac{1}{4} \sin^2 \beta \sin^2 \frac{\beta}{2} - \frac{1}{2} \sin^2(\beta) \cos^2 \left(\frac{\beta}{2} \right) \\
k_2^\beta &= \cos^2 \frac{\beta}{2} \sin^2 \beta \\
k_3^\beta &= \frac{1}{4} \sin^2(\beta) \cos^2 \left(\frac{\beta}{2} \right) + \sin^6 \left(\frac{\beta}{2} \right) + \frac{1}{2} \sin^2 \left(\frac{\beta}{2} \right) \sin^2(\beta) \\
k_4^\beta &= 2 \sin(\beta) \cos^4 \left(\frac{\beta}{2} \right) - \frac{1}{2} \sin^3(\beta) \\
k_5^\beta &= \sin(\beta) \cos^4 \left(\frac{\beta}{2} \right) - \sin^4 \left(\frac{\beta}{2} \right) \sin(\beta) \\
k_6^\beta &= \sin^2(\beta).
\end{aligned} \tag{D9}$$

In the above derivation, we have used the following identities in addition to those in Eqs. (D4) and (D5):

$$\begin{aligned}
S_{AB}^+ S_{AB}^- &= -S_{AB}^- S_{AB}^+ = \frac{1}{2} (Z_A - Z_B), \\
S_{AB}^+ S_{AB}^+ &= -S_{AB}^- S_{AB}^- = \frac{1}{2} (\mathbb{1} - Z_A Z_B) \\
S_{BC}^- S_{AB}^- &= \frac{1}{2} S_{AC}^+ - \frac{1}{2} S_{AC}^- Z_B, \quad S_{BC}^+ S_{AB}^+ = \frac{1}{2} S_{AC}^+ - \frac{1}{2} S_{AC}^- Z_B \\
S_{AB}^- S_{BC}^- &= S_{AB}^- S_{BC}^- Z_A Z_B = \frac{1}{2} S_{AC}^- Z_B + \frac{1}{2} S_{AC}^+ \\
S_{AB}^- S_{BC}^- S_{AB}^- &= 0.
\end{aligned} \tag{D10}$$

In Eq. (D8), the support $\mathbb{1}, Z_A Z_B, Z_B Z_C$ leave the occupations of the computational basis states invariant, the support $S_{AB}^-, S_{BC}^-, S_{AC}^+$ varies the occupations, and the parameter β controls the magnitude of the change of total superposition. The decomposed supports are linearly independent of each other. In Eq. (D8), we observe in addition to the expected support on S_{AB}^- and S_{BC}^- as shown directly in the circuit Fig. 15(b), the two $e^{\beta S_{BC}^-}$ operators in $e^{\beta S_{BC}^-} e^{\beta S_{AB}^-} e^{\beta S_{BC}^-}$ act as a bridge to generate support on S_{AC}^+ , and we name this phenomenon as the quantum bridge on two-qubit excitations. In fact, this result, generating new support, can also be extended to additional ancilla by repeatedly sandwiching the circuit with additional two-qubit excitation operators.

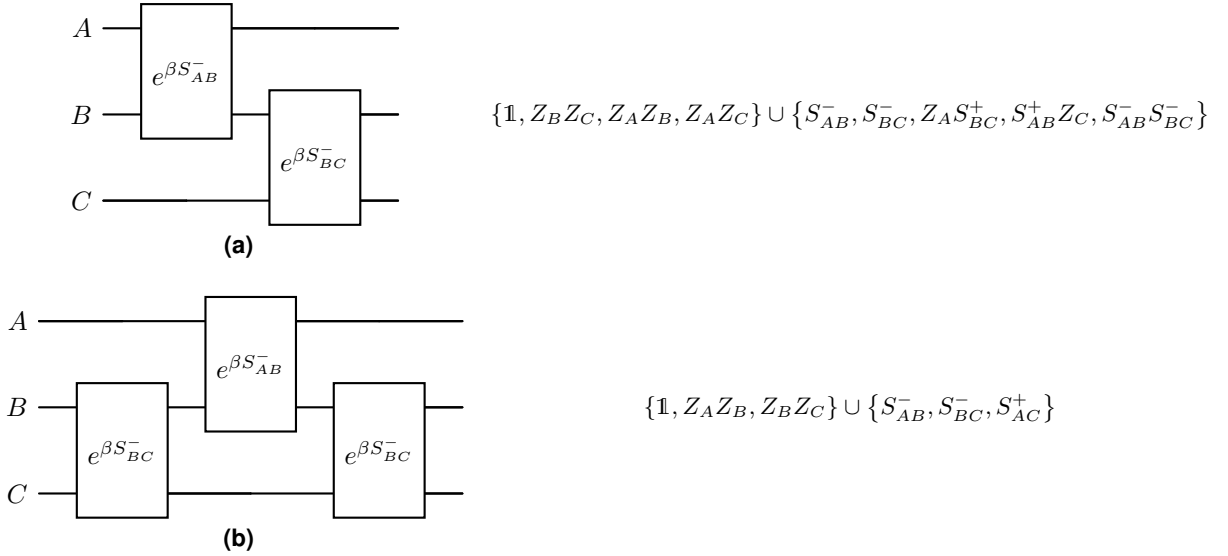


Figure 15. Quantum circuit diagrams of (a) $e^{\beta S_{AB}^-} e^{\beta S_{BC}^-}$ and (b) $e^{\beta S_{BC}^-} e^{\beta S_{AB}^-} e^{\beta S_{BC}^-}$. The set on the right of each circuit is the linear independent support of the unitary generated by the quantum circuit. These operators form an orthogonal basis for the subspace with respect to the Hilbert-Schmidt inner product. The first set includes operators that leave the occupation of computational basis states invariant. The second set includes operators that vary the occupation.

Appendix E: Quantum bridge on three-qubit excitations

In this appendix, we analyse the action of three-qubit excitations. Similar to the two-qubit excitation, for the three-qubit excitation operator as in Eq. (25), we can define a pair of operators:

$$P_{ABC}^\pm := Q_A^\dagger Q_B Q_C \pm Q_A Q_B^\dagger Q_C^\dagger. \tag{E1}$$

In the Pauli basis, these operators are

$$P_{ABC}^+ = \frac{1}{4} (X_A X_B X_C + Y_A X_B Y_C - X_A Y_B Y_C + Y_A Y_B X_C), \tag{E2}$$

$$P_{ABC}^- = \frac{i}{4} (X_A X_B Y_C + X_A Y_B X_C - Y_A X_B X_C + Y_A Y_B Y_C). \tag{E3}$$

Notice P_{ABC}^\pm is invariant under swapping the B and C indices. Applying Pauli- Z operators we find the following identities:

$$\begin{aligned}
P_{ABC}^+ Z_A &= -Z_A P_{ABC}^+ = P_{ABC}^- \\
P_{ABC}^+ Z_B &= P_{ABC}^+ Z_C = -Z_B P_{ABC}^+ = -Z_C P_{ABC}^+ = -P_{ABC}^- \\
P_{ABC}^+ Z_A Z_B &= P_{ABC}^+ Z_A Z_C = Z_A Z_B P_{ABC}^+ = Z_A Z_C P_{ABC}^+ = -P_{ABC}^+ \\
P_{ABC}^+ Z_B Z_C &= Z_B Z_C P_{ABC}^+ = P_{ABC}^+ \\
P_{ABC}^+ Z_A Z_B Z_C &= Z_A Z_B Z_C P_{ABC}^+ = P_{ABC}^-.
\end{aligned} \tag{E4}$$

Now we will use these identities to express the circuit in Fig. 16(a):

$$\begin{aligned}
& e^{\beta S_{CD}^-} e^{\beta P_{ABC}^-} e^{\beta S_{CD}^-} \\
&= \left(\cos^2 \left(\frac{\beta}{2} \right) \mathbb{1} + \sin^2 \left(\frac{\beta}{2} \right) Z_C Z_D + \sin(\beta) S_{CD}^- \right) \\
&\quad \left(\frac{1}{4} (3 + \cos(\beta)) \mathbb{1}_{ABC} + \frac{1}{2} \sin^2 \left(\frac{\beta}{2} \right) (Z_A Z_B + Z_A Z_C - Z_B Z_C) + \sin(\beta) P_{ABC}^- \right) \\
&\quad \left(\cos^2 \left(\frac{\beta}{2} \right) \mathbb{1} + \sin^2 \left(\frac{\beta}{2} \right) Z_C Z_D + \sin(\beta) S_{CD}^- \right) \\
&= \left(\frac{1}{4} \cos^2 \left(\frac{\beta}{2} \right) (3 + \cos(\beta)) \mathbb{1} + \frac{1}{4} (3 + \cos(\beta)) \sin^2 \left(\frac{\beta}{2} \right) Z_C Z_D + \frac{1}{4} (3 + \cos(\beta)) \sin(\beta) S_{CD}^- \right. \\
&\quad \left. + \frac{1}{8} \sin^2(\beta) (Z_A Z_B + Z_A Z_C - Z_B Z_C) + \frac{1}{2} \sin^4 \left(\frac{\beta}{2} \right) (Z_A Z_B Z_C Z_D + Z_A Z_D - Z_B Z_D) \right. \\
&\quad \left. + \frac{1}{2} \sin^2 \left(\frac{\beta}{2} \right) \sin(\beta) (S_{CD}^- Z_A Z_B + S_{CD}^+ Z_A - S_{CD}^+ Z_B) \right. \\
&\quad \left. + \cos^2 \left(\frac{\beta}{2} \right) \sin(\beta) P_{ABC}^- + \sin^2 \left(\frac{\beta}{2} \right) \sin(\beta) P_{ABC}^+ Z_D + \sin^2(\beta) S_{CD}^- P_{ABC}^- \right) \\
&\quad \left(\cos^2 \left(\frac{\beta}{2} \right) \mathbb{1} + \sin^2 \left(\frac{\beta}{2} \right) Z_C Z_D + \sin(\beta) S_{CD}^- \right) \\
&= m_1^\beta \mathbb{1} + m_2^\beta Z_A Z_B + m_3^\beta Z_C Z_D + m_4^\beta Z_A Z_C + m_5^\beta Z_B Z_C + m_6^\beta Z_A Z_B Z_C Z_D \\
&\quad + m_7^\beta S_{CD}^- + m_8^\beta Z_A Z_B S_{CD}^- + m_9^\beta P_{ABC}^- + m_{10}^\beta P_{ABD}^+,
\end{aligned} \tag{E5}$$

where

$$\begin{aligned}
m_1^\beta &= \frac{1}{4} (3 + \cos(\beta)) \left(\frac{1}{4} (3 + \cos(2\beta)) - \frac{1}{2} \sin^2(\beta) \right), \\
m_2^\beta &= \frac{1}{2} \sin^6 \left(\frac{\beta}{2} \right) + \frac{1}{8} \sin^2(\beta) \cos^2 \left(\frac{\beta}{2} \right) - \frac{1}{4} \sin^2 \left(\frac{\beta}{2} \right) \sin^2(\beta), \\
m_3^\beta &= \frac{1}{4} \sin^2(\beta) (3 + \cos(\beta)), \\
m_4^\beta &= \frac{1}{8} \sin^2(\beta) \cos^2 \left(\frac{\beta}{2} \right) + \frac{1}{2} \sin^6 \left(\frac{\beta}{2} \right) + \frac{1}{4} \sin^2 \left(\frac{\beta}{2} \right) \sin^2(\beta), \\
m_5^\beta &= -\frac{1}{8} \sin^2(\beta) \cos^2 \left(\frac{\beta}{2} \right) - \frac{1}{2} \sin^6 \left(\frac{\beta}{2} \right) - \frac{1}{4} \sin^2 \left(\frac{\beta}{2} \right) \sin^2(\beta), \\
m_6^\beta &= \frac{1}{2} \sin^2 \left(\frac{\beta}{2} \right) \sin^2(\beta), m_7^\beta = \frac{1}{4} (3 + \cos(\beta)) \sin(2\beta) \\
m_8^\beta &= \frac{1}{4} \sin^3(\beta) - \sin^4 \left(\frac{\beta}{2} \right) \sin(\beta), m_9^\beta = \cos(\beta) \sin(\beta), m_{10}^\beta = \sin^2(\beta).
\end{aligned} \tag{E6}$$

In the above derivation, we have used the following identities in addition to those in Eq. (E4):

$$\begin{aligned}
S_{CD}^- P_{ABC}^- &= \frac{1}{2}(P_{ABD}^+ - Z_C P_{ABD}^-) \\
P_{ABC}^- S_{CD}^- &= \frac{1}{2}(P_{ABD}^+ + Z_C P_{ABD}^-) \\
P_{ABC}^+ S_{CD}^+ &= (-P_{ABC}^- Z_C)(-Z_C S_{CD}^-) = P_{ABC}^- S_{CD}^- = \frac{1}{2}(P_{ABD}^+ + Z_C P_{ABD}^-) \\
S_{CD}^- P_{ABC}^- S_{CD}^- &= \frac{1}{2}(P_{ABD}^+ - Z_C P_{ABD}^-) S_{CD}^- \\
&= \frac{1}{2}(P_{ABD}^+ S_{CD}^- - P_{ABD}^- Z_C S_{CD}^-) \\
&= \frac{1}{2}(-P_{ABD}^- Z_D S_{CD}^- - P_{ABD}^- Z_C S_{CD}^-) \\
&= \frac{1}{2}(-P_{ABD}^- S_{CD}^+ - P_{ABD}^- (-S_{CD}^+)) = 0.
\end{aligned} \tag{E7}$$

In Eq. (E5), the support $\mathbb{1}, Z_A Z_B, Z_C Z_D, Z_A Z_C, Z_B Z_C, Z_A Z_B Z_C Z_D$ leave the occupations of the computational basis states invariant, the support $S_{CD}^-, Z_A Z_B S_{CD}^-, P_{ABC}^-, P_{ABD}^+$ varies the occupations, and the parameter β controls the magnitude of the change of the total superposition. The decomposed supports are linearly independent of each other. Thus, $e^{\beta S_{CD}^-} e^{\beta P_{ABC}^-} e^{\beta S_{CD}^-}$ has support on P_{ABD}^+ in addition to the expected support on P_{ABC}^- and S_{CD}^- and local phase generating terms. The same derivation follows directly for $e^{\beta S_{BD}^-} e^{\beta P_{ABC}^-} e^{\beta S_{BD}^-}$ [see Fig. 16(b)] as P_{ABC}^- is invariant under exchange of the indices B and C .

Next we consider the circuit in Fig. 16(c):

$$\begin{aligned}
&e^{\beta S_{AD}^-} e^{\beta P_{ABC}^-} e^{\beta S_{AD}^-} \\
&= \left(\cos^2 \left(\frac{\beta}{2} \right) \mathbb{1} + \sin^2 \left(\frac{\beta}{2} \right) Z_A Z_D + \sin(\beta) S_{AD}^- \right) \\
&\quad \left(\frac{1}{4} (3 + \cos(\beta)) \mathbb{1}_{ABC} + \frac{1}{2} \sin^2 \left(\frac{\beta}{2} \right) (Z_A Z_B + Z_A Z_C - Z_B Z_C) + \sin(\beta) P_{ABC}^- \right) \\
&\quad \left(\cos^2 \left(\frac{\beta}{2} \right) \mathbb{1} + \sin^2 \left(\frac{\beta}{2} \right) Z_A Z_D + \sin(\beta) S_{AD}^- \right) \\
&= \left(\frac{1}{4} \cos^2 \left(\frac{\beta}{2} \right) (3 + \cos(\beta)) \mathbb{1} + \frac{1}{4} (3 + \cos(\beta)) \sin^2 \left(\frac{\beta}{2} \right) Z_A Z_D + \frac{1}{4} (3 + \cos(\beta)) \sin(\beta) S_{AD}^- \right. \\
&\quad \left. + \frac{1}{8} \sin^2(\beta) (Z_A Z_B + Z_A Z_C - Z_B Z_C) + \frac{1}{2} \sin^4 \left(\frac{\beta}{2} \right) (Z_B Z_D - Z_C Z_D - Z_A Z_B Z_C Z_D) \right. \\
&\quad \left. + \frac{1}{2} \sin^2 \left(\frac{\beta}{2} \right) \sin(\beta) (S_{AD}^+ Z_B + S_{AD}^+ Z_C - S_{AD}^- Z_B Z_C) \right. \\
&\quad \left. + \cos^2 \left(\frac{\beta}{2} \right) \sin(\beta) P_{ABC}^- - \sin^2 \left(\frac{\beta}{2} \right) \sin(\beta) P_{ABC}^+ Z_D + \sin^2(\beta) S_{AD}^- P_{ABC}^- \right) \\
&\quad \left(\cos^2 \left(\frac{\beta}{2} \right) \mathbb{1} + \sin^2 \left(\frac{\beta}{2} \right) Z_A Z_D + \sin(\beta) S_{AD}^- \right) \\
&= m_1^\beta \mathbb{1} + m_2^\beta Z_B Z_C + m_3^\beta Z_A Z_D + m_4^\beta Z_A Z_B + m_5^\beta Z_A Z_C + m_6^\beta Z_A Z_B Z_C Z_D \\
&\quad + m_7^\beta S_{AD}^- + m_8^\beta Z_B Z_C S_{AD}^- + m_9^\beta P_{ABC}^- + m_{10}^\beta P_{DBC}^+,
\end{aligned} \tag{E8}$$

where

$$\begin{aligned}
m_1^\beta &= \frac{1}{4}(3 + \cos(\beta))\left(\frac{1}{4}(3 + \cos(2\beta)) - \frac{1}{2}\sin^2(\beta)\right), \\
m_2^\beta &= -\frac{1}{2}\sin^6\left(\frac{\beta}{2}\right) - \frac{1}{8}\sin^2(\beta)\cos^2\left(\frac{\beta}{2}\right) + \frac{1}{4}\sin^2\left(\frac{\beta}{2}\right)\sin^2(\beta), \\
m_3^\beta &= \frac{1}{4}\sin^2(\beta)(3 + \cos(\beta)), \\
m_4^\beta &= \frac{1}{8}\sin^2(\beta)\cos^2\left(\frac{\beta}{2}\right) + \frac{1}{2}\sin^6\left(\frac{\beta}{2}\right) + \frac{1}{4}\sin^2\left(\frac{\beta}{2}\right)\sin^2(\beta), \\
m_5^\beta &= \frac{1}{8}\sin^2(\beta)\cos^2\left(\frac{\beta}{2}\right) + \frac{1}{2}\sin^6\left(\frac{\beta}{2}\right) + \frac{1}{4}\sin^2\left(\frac{\beta}{2}\right)\sin^2(\beta), \\
m_6^\beta &= -\frac{1}{2}\sin^2\left(\frac{\beta}{2}\right)\sin^2(\beta), m_7^\beta = \frac{1}{4}(3 + \cos(\beta))\sin(2\beta) \\
m_8^\beta &= -\frac{1}{4}\sin^3(\beta) + \sin^4\left(\frac{\beta}{2}\right)\sin(\beta), m_9^\beta = \cos(\beta)\sin(\beta), m_{10}^\beta = -\sin^2(\beta).
\end{aligned} \tag{E9}$$

In the above derivation, we have used the following identities in addition to those in Eq. (E4) and Eq. (E7):

$$\begin{aligned}
P_{ABC}^- S_{AD}^- &= \frac{1}{2}(Z_A P_{DBC}^- - P_{DBC}^+) \\
S_{AD}^- P_{ABC}^- &= -\frac{1}{2}(Z_A P_{DBC}^- + P_{DBC}^+) \\
P_{ABC}^+ S_{AD}^+ &= (P_{ABC}^- Z_A)(-Z_A S_{AD}^-) = -P_{ABC}^- S_{AD}^- \\
S_{AD}^+ P_{ABC}^+ &= (-S_{AD}^- Z_A)(-Z_A P_{ABC}^-) = S_{AD}^- P_{ABC}^- \\
S_{AD}^- P_{ABC}^- S_{AD}^- &= 0.
\end{aligned} \tag{E10}$$

In Eq. (E8), the support $\mathbb{1}, Z_B Z_C, Z_A Z_D, Z_A Z_B, Z_A Z_C, Z_A Z_B Z_C Z_D$ leave the occupations of the computational basis states invariant, the support $S_{AD}^-, Z_B Z_C S_{AD}^-, P_{ABC}^-, P_{DBC}^+$ vary the occupations, and the parameter β controls the magnitude of the change the total superposition. The decomposed supports are linearly independent of each other. Thus, $e^{\beta S_{AD}^-} e^{\beta P_{ABC}^-} e^{\beta S_{AD}^-}$ has support on P_{DBC}^+ in addition to the expected support on P_{ABC}^- and S_{AD}^- and local phase generating terms.

In this appendix, we have shown that by sandwiching a three-qubit excitation with two-qubit excitations that act non-trivially on an ancilla qubit, the resulting unitary will have support on a three-qubit excitation acting upon this ancilla qubit. We name this phenomenon as the quantum bridge on three-qubit excitations.

§§

Appendix F: Mixing operator with a implement of quantum bridges

In this appendix, we show how the design of the mixing operator $H_{tt'}(\beta)$ (see in Sec. IID) utilises the quantum bridges to reduce the cost of quantum resources and generate sufficient support for binary arithmetic operations between asset blocks. By using the same notation as in Sec. IID, we have

$$\begin{aligned}
& [S_{tt'}^k, P_{ttt'}^k] \\
&= \left[\frac{i}{2} (X_t^k Y_{t'}^k - Y_t^k X_{t'}^k), \frac{i}{4} (X_t^{k+1} X_t^k Y_{t'}^k + X_t^{k+1} Y_t^k X_{t'}^k - Y_t^{k+1} X_t^k X_{t'}^k + Y_t^{k+1} Y_t^k Y_{t'}^k) \right] \\
&= -\frac{1}{8} \{ [X_t^k Y_{t'}^k, X_t^{k+1} X_t^k Y_{t'}^k] + [X_t^k Y_{t'}^k, X_t^{k+1} Y_t^k X_{t'}^k] - [X_t^k Y_{t'}^k, Y_t^{k+1} X_t^k X_{t'}^k] + [X_t^k Y_{t'}^k, Y_t^{k+1} Y_t^k Y_{t'}^k] \\
&\quad - [Y_t^k X_{t'}^k, X_t^{k+1} X_t^k Y_{t'}^k] - [Y_t^k X_{t'}^k, X_t^{k+1} Y_t^k X_{t'}^k] + [Y_t^k X_{t'}^k, Y_t^{k+1} X_t^k X_{t'}^k] - [Y_t^k X_{t'}^k, Y_t^{k+1} Y_t^k Y_{t'}^k] \} \\
&= -\frac{1}{8} \{ X_t^{k+1} + X_t^{k+1} [X_t^k Y_{t'}^k, Y_t^k X_{t'}^k] - Y_t^{k+1} [Y_{t'}^k, X_{t'}^k] + Y_t^{k+1} [X_t^k, Y_t^k] \\
&\quad - X_t^{k+1} [Y_t^k X_{t'}^k, X_t^k Y_{t'}^k] - X_t^{k+1} + Y_t^{k+1} [Y_t^k, X_t^k] - Y_t^{k+1} [X_{t'}^k, Y_{t'}^k] \} \\
&= 0
\end{aligned} \tag{F1}$$

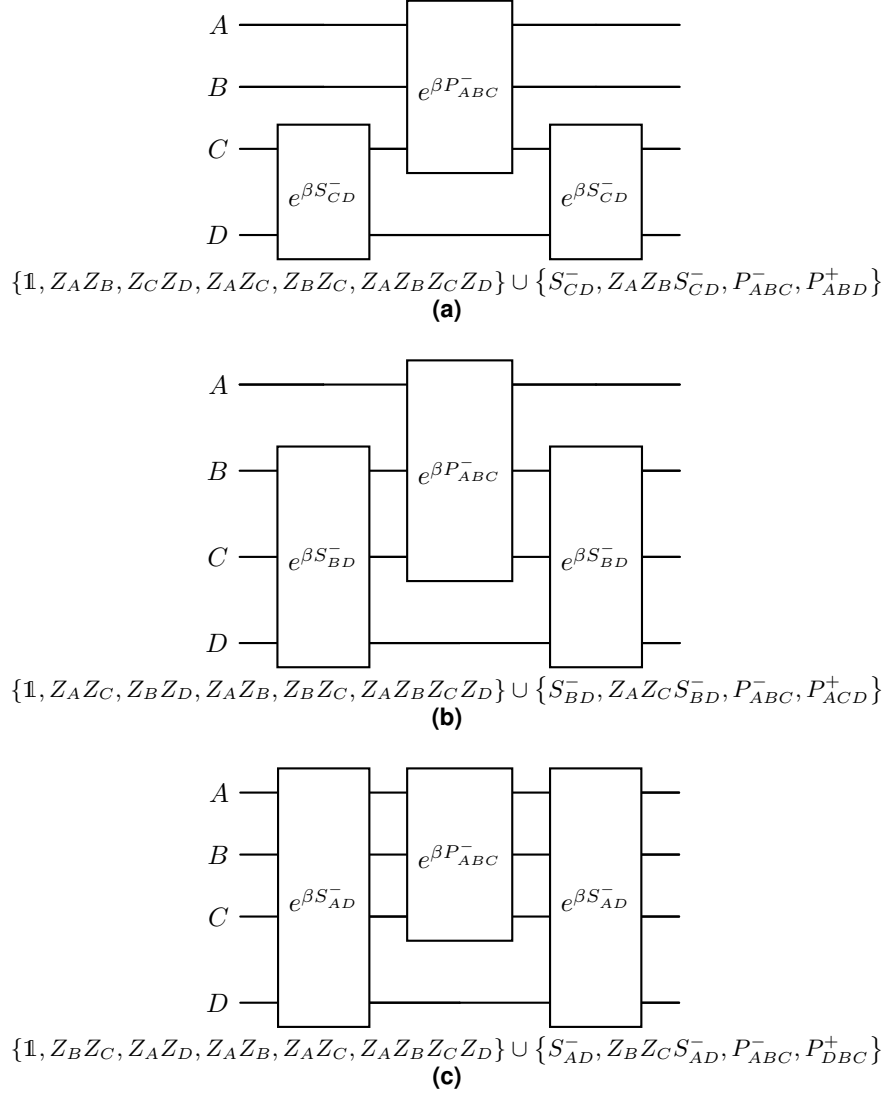


Figure 16. Quantum circuits of (a) $e^{\beta S_{CD}^-} e^{\beta P_{ABC}^-} e^{\beta S_{CD}^-}$, (b) $e^{\beta S_{BD}^-} e^{\beta P_{ABC}^-} e^{\beta S_{BD}^-}$, and (c) $e^{\beta S_{AD}^-} e^{\beta P_{ABC}^-} e^{\beta S_{AD}^-}$. The set on the right of each circuit is the linear independent support of the unitary generated by the quantum circuit. These operators form an orthogonal basis for the subspace with respect to the Hilbert-Schmidt inner product. The first set includes operators that leave the occupation of computational basis states invariant. The second set includes operators that vary the occupation.

where the second equality follows from $[A + B, C + D] = [A, C] + [B, C] + [A, D] + [B, D]$ and $[c_1 A, c_2 B] = c_1 c_2 [A, B]$ with $c_1, c_2 \in \mathbb{C}$, for the third equality we use the fact that Pauli operators are involutions, and the last equality follows from $[XY, YX] = [YX, XY]$. Thus, we have

$$\begin{aligned}
 & e^{-i\beta S_{tt'}^k} e^{-i\beta P_{ttt'}^k} \\
 &= e^{-i\beta S_{tt'}^k - i\beta P_{ttt'}^k} \\
 &= e^{-i\beta P_{ttt'}^k} e^{-i\beta S_{tt'}^k}
 \end{aligned} \tag{F2}$$

Then, Eq. (32) can be expanded as

$$\begin{aligned}
& H_{tt'}(\beta) \\
&= \tilde{S}_{tt'}(\beta) \tilde{P}_{tt'}^e(\beta) \tilde{P}_{tt'}^o(\beta) \tilde{S}_{tt'}(\beta) \\
&= \left(\bigotimes_{k=1}^l e^{-i\beta S_{tt'}^k} \right) \left(\bigotimes_{k \in \mathcal{K}_1} e^{-i\beta P_{ttt'}^k} \right) \left(\bigotimes_{k \in \mathcal{K}_2} e^{-i\beta P_{ttt'}^k} \right) \left(\bigotimes_{k=1}^l e^{-i\beta S_{tt'}^k} \right) \\
&= \left(\bigotimes_{k \in \mathcal{K}_2} e^{-i\beta S_{tt'}^k} \right) \left(\bigotimes_{k \in \mathcal{K}_1} e^{-i\beta P_{ttt'}^k} \right) \left(\bigotimes_{k=1}^l e^{-i\beta S_{tt'}^k} \right) \left(\bigotimes_{k \in \mathcal{K}_2} e^{-i\beta P_{ttt'}^k} \right) \left(\bigotimes_{k \in \mathcal{K}_1} e^{-i\beta S_{tt'}^k} \right) \\
&= \left(\bigotimes_{k \in \mathcal{K}_2} e^{-i\beta S_{tt'}^k} \right) \left(\bigotimes_{k \in \mathcal{K}_1} e^{-i\beta P_{ttt'}^k} \right) \left(\bigotimes_{k \in \mathcal{K}_2} e^{-i\beta S_{tt'}^k} \right) \left(\bigotimes_{k \in \mathcal{K}_1} e^{-i\beta S_{tt'}^k} \right) \\
&\quad \left(\bigotimes_{k \in \mathcal{K}_2} e^{-i\beta P_{ttt'}^k} \right) \left(\bigotimes_{k \in \mathcal{K}_1} e^{-i\beta S_{tt'}^k} \right) \\
&= e^{-i\beta S_{tt'}^1} \left(\bigotimes_{k \in \mathcal{K}_1} e^{-i\beta S_{tt'}^{k+1}} e^{-i\beta P_{ttt'}^k} e^{-i\beta S_{tt'}^{k+1}} \right) e^{-i\beta S_{tt'}^1} \left(\bigotimes_{k \in \mathcal{K}_2} e^{-i\beta S_{tt'}^k} e^{-i\beta P_{ttt'}^k} e^{-i\beta S_{tt'}^k} \right)
\end{aligned} \tag{F3}$$

where $\mathcal{K}_1, \mathcal{K}_2$ are defined in Eq. (33) and the third equality follows from Eq. (F2).

The tensor product over \mathcal{K}_2 has support on all $S_{tt'}^k$, $P_{ttt'}^k$ and $P_{ttt'}^k$ with $k \in \mathcal{K}_2$. As $e^{-i\beta S_{tt'}^1}$ has support on the identity then the support from the tensor product over \mathcal{K}_2 is not lost. In addition $e^{-i\beta S_{tt'}^1}$ yields support on $S_{tt'}^1$. Next, the tensor product over \mathcal{K}_1 has support on the identity so all prior support is retained. In addition we gain support on all $S_{tt'}^k$, $P_{ttt'}^k$ and $P_{ttt'}^k$ with $k \in \mathcal{K}_1$. Then, the factor $e^{-i\beta S_{tt'}^1}$ once again retains all prior support as it has support on the identity. Finally, all support in Eq. (F3) include the binary arithmetic operations between t and t' asset block as introduced in the Sec. IID. Changing the parameter β will influence the coefficients of the unitary on the support and thus control the supposition of the computational basis state.

Appendix G: Simulation on qubit excitation mixing operator with different L

In this appendix, we compare mixing operator $\hat{M}_L(\beta)$ with $L = 1, 2$ provided in Sec. IID. We observe the loss landscapes corresponding to $\hat{M}_1(\beta)$ have larger gradients, fewer and deeper valleys with roughly the same minimum value as $\hat{M}_2(\beta)$ —see data in Table I. A representative example is shown in Fig. 17(left). We also find that the ansatz becomes harder to optimise in the presence of stochastic measurement errors when using $\hat{M}_2(\beta)$ compared to $\hat{M}_1(\beta)$ —see Fig. 17(right). In Sec. IID, we demonstrate that the ansatz wavefunction generated by $\hat{M}_2(\beta)$ is a superposition with support on more computational basis vectors than generated by $\hat{M}_1(\beta)$. The increased support generated by $\hat{M}_2(\beta)$ suggests that as β is varied, the total variation in any given occupation will be less sensitive to β . Thus, we conjecture, this reduces the gradients with respect to β and makes the optimisation harder in the presence of stochastic measurement errors. Therefore, we primarily use $\hat{M}_1(\beta)$ as our mixing operator.

Mixing Operator	Average Gradient	Largest Gradient	Min	Max–Min	Valleys
$\hat{M}_1(\beta)$	0.0298 ± 0.0025	0.132 ± 0.011	0.220 ± 0.028	0.051 ± 0.003	4.2 ± 0.1
$\hat{M}_2(\beta)$	0.0226 ± 0.0024	0.101 ± 0.010	0.220 ± 0.028	0.022 ± 0.002	6.3 ± 0.1

Table I. Tabulated properties of the loss landscapes of mixing operators $\hat{M}_L(\beta)$ with $L = 1, 2$. The data is collected from 100 simulations each using randomly generated DGMVP instances with the asset number $n = 4$ and the asset binary block length $l = 5$. In our simulations, we use the $|\mathbf{w}\rangle_{mb}$ as the initial state and a $p = 10$ layer ansatz. We scan the landscape of the fifth mixing operator's parameter $\beta_5 \in [0, 2\pi]$ with a resolution of $\pi/500$ and fix all the other ansatz parameters as $\pi/4$. Each data point is estimated with $N_M = 2^{22} = 4194304$ measurement shots. The average (second column) and largest (third column) gradient magnitudes of the approximation ratio are calculated using finite differences. The minimum (fourth column), maximum–minimum (fifth column), and the number of valleys (sixth column) are averaged over the 100 instances. All values for $\hat{M}_1(\beta)$ and $\hat{M}_2(\beta)$ are separated by more than the standard error in the mean except for the minimum (bold).

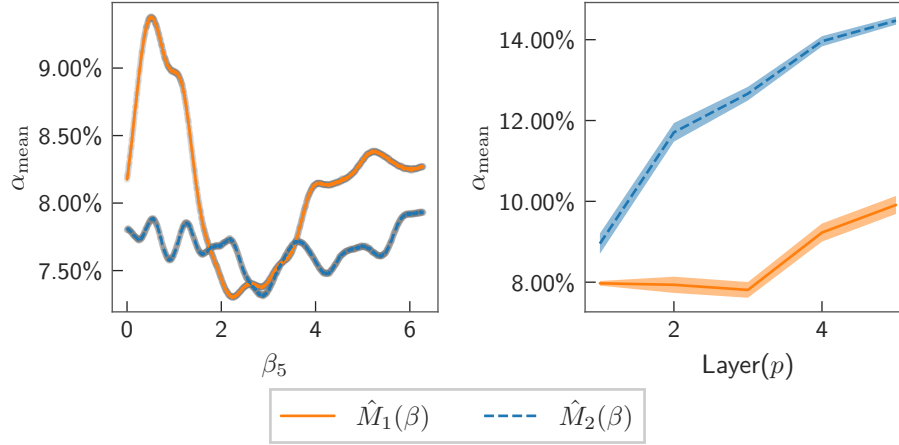


Figure 17. A comparison of the mixing operators $\hat{M}_1(\beta)$ and $\hat{M}_2(\beta)$. The left panel shows a typical loss landscape of the parameter, $\beta_5 \in [0, 2\pi]$, of the fifth mixing operator with a resolution of $\pi/500$ with all the other ansatz parameters fixed as $\pi/4$. In our simulations, we use the $|\mathbf{w}\rangle_{mb}$ as the initial state and a $p = 10$ layer ansatz. Each plotted point is estimated with $N_M = 2^{22} = 4194304$ measurement shots. The thin grey shadow beneath the coloured lines represents ensembles of estimations, each using $N_M = 2^{22} = 4194304$ measurement shots to indicate the stochastic noise. The right panel depicts α_{mean} for the fixed ansatz approach with the $|\mathbf{w}\rangle_{rd}$ initial state as a function of the number of layers p . The initial parameters β, γ are sampled from a uniform distribution. We utilise COBYLA as the optimiser with $N_m = 2^{10} = 1024$, and post-optimisation measurements $N_M = 2^{16} = 65536$. The shaded regions denote standard error in the mean. For both panels, the asset number $n = 4$ and the asset binary block length $l = 5$.

Appendix H: Comparison on the comparison of COBYLA and DA

In this appendix, we show a collection of statistical simulations that compare the optimisation performance of COBYLA and DA when optimising multilayered ansätze. In Fig. 18(a), the number of cost function access N_f of COBYLA increases linearly with p , while DA consumes roughly a constant number of cost function accesses because we set a fixed \mathcal{I} for DA. Note that \mathcal{I} is a soft constraint and can be slightly exceeded as we allow the final optimiser iteration in the local search to complete after the maximal \mathcal{I} is violated. We observe that DA uses fewer total cost function accesses than COBYLA to achieve smaller values of α_{\min} and α_{mean} in the large p regime. We also observe in Fig. 18(b)(c) that DA is robust to stochastic measurement noise as it achieves a lower α_{mean} and a much lower α_{\min} for nearly all examined p . The experiment shows the advantages of using DA to reduce the cost of quantum resources in optimising parameterised quantum circuits.

Appendix I: Further investigations of the hyperparameters impact on performance of DA's optimisation

To investigate the performance and identify the best parameters for DA, we compared DA's optimisation performance by varying \mathcal{I} and N_m . We consider two methods for fixing \mathcal{I} : constant \mathcal{I} and linear growth (LG) in which $\mathcal{I} = 5000p$. However, we allow the DA to complete its final local search after the maximal \mathcal{I} is violated, and so \mathcal{I} can be slightly exceeded.

In Fig. 19(a), the LG line shows a constant plateau with $p \geq 2$ demonstrating sufficient \mathcal{I} and N_m will stabilise the optimisation. The upward trend with constant \mathcal{I} is discussed in Appx. C. When decreasing \mathcal{I} and N_m , we observe the optimised α_{mean} will be in general higher, and α_{mean} increases with increasing p .

However, we are interested in the region with small \mathcal{I} and N_m where achieving the real quantum advantage may be possible. By fixing $\mathcal{I} = 2000$ (the dashed lines with round markers in Fig. 19, we find that increasing N_m from 4 to 8 and 8 to 16 improves α_{mean} roughly the same amount as increasing N_m from 16 to 1024. Thus, we observe the decrease of α_{mean} with increasing N_m starts to plateau. Now fixing $N_m = 16$ (see the dark-green lines in Fig. 19), we observe decreasing \mathcal{I} from 5000 to 2000 has little impact of α_{\min} but a further decrease to 100 is extremely detrimental. Thus, after 2000 expectation value estimations, the improvement per expectation value estimation is relatively small. Thus further optimisation is expensive in expectation value estimations.

Another metric of importance is α_{\min} , see Fig. 19(b). We observe that α_{\min} often has a local maximum around $p = 2$ but generally decreases with increasing p . As was observed in Appx. C, the parameters of the best α_{mean} do not

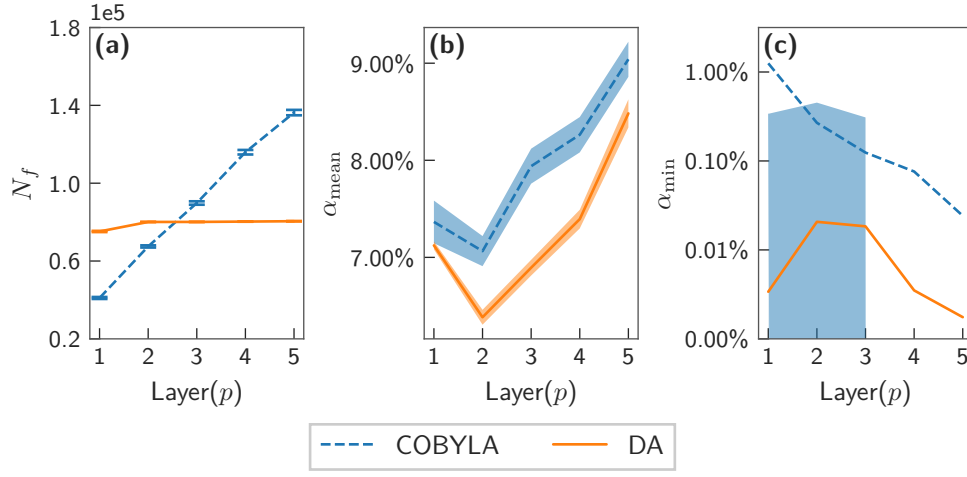


Figure 18. A performance comparison between DA and COBYLA. The panels from left to right show (a) N_f , (b) α_{mean} , and (c) α_{min} as a function of p . The results are averaged over 100 simulations with random initial ansatz parameters. We plot α_{min} on a log scale to emphasise the exponential decay. The blue dash line is the COBYLA optimised sample mean with $N_m = 2^{10} = 1024$, the orange solid line is the optimised sample mean of DA with $\mathcal{I} = 5000$ and $N_m = 2^4 = 16$. The error bar in (a) is induced by the expectation value estimations access, and the shaded region in (b) and (c) indicates the 25% to 75% percentile of data. These simulations use the mixing operator $\hat{M}_1(\beta)$ and the initial state $|\mathbf{w}\rangle_{mb}$ with $n = l = 4$. The optimisation method is the fix ansatz approach for every ps with the final expectation value measurement shots $N_M = 2^{16} = 65536$.

correspond to the best α_{min} directly. Thus, focusing on optimising only one ratio may lead to the detriment of the other. We find that the choice of $\mathcal{I} = 2000$ and $N_m = 16$ for DA is a good trade-off between the optimisation costs (\mathcal{I} and N_m) and the optimisation performance as indicated by α_{mean} and α_{min} for the values of n and l considered in this article.

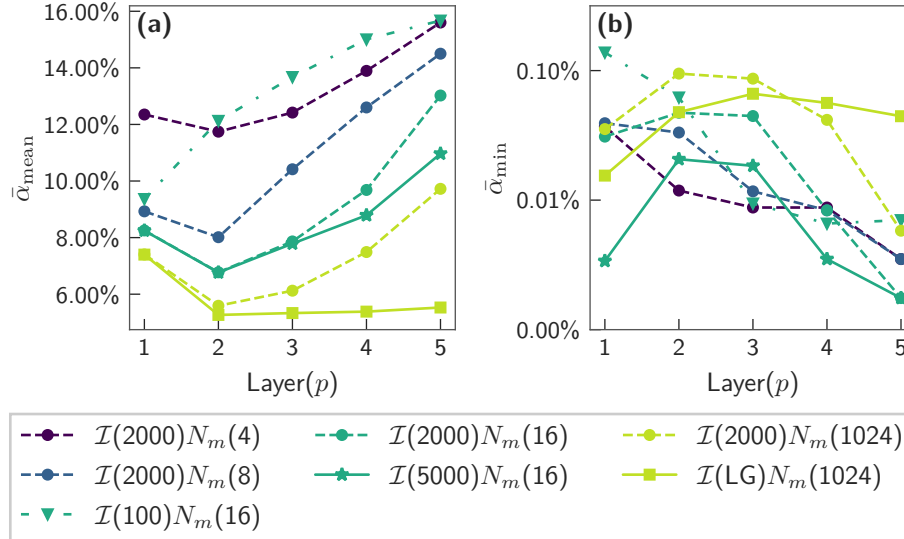


Figure 19. A comparison of hyperparameters \mathcal{I} and N_m impact on the performance of DA's optimisation as a function of the layer p : (a) α_{mean} , (b) α_{min} . Every line in the graphs is the average over 100 simulations with random initial parameters. These simulations use the initial state $|\mathbf{w}\rangle_{mb}$ and the mixing operator $\hat{M}_1(\beta)$ with $n = l = 4$. The optimisation method is the fix ansatz approach for every ps with the final expectation value measurement shots $N_M = 2^{16} = 65536$.

Appendix J: Simulation on binary block length and asset size scaling

To investigate the scaling of our quantum algorithm for solving the DGMVP, we combine the most efficient methods from previous simulations to perform stochastic simulations on problem sets with varied binary block lengths l and the number of assets n . For each l and n our simulations contain covariance matrices generated from randomly selected US stocks—see Appx. A. For the ansatz circuit, we use $\hat{M}_1(\beta)$ as the mixing operator—see Appx. G. In this appendix, we compare the performance of the initial states $|\mathbf{w}\rangle_{ws}$ and $|\mathbf{w}\rangle_{mb}$. We apply an unfrozen-layerwise optimisation method (see Secs. III A and III B) up to $p = 5$ layers using DA as the classical optimiser. DA uses $N_m = 16$ shots for estimating expectation value during optimisation with a soft constraint $\mathcal{I} = 2000$ expectation value estimations for each newly added layer. All results are obtained by reconstructing the statevectors with optimised parameters to remove the stochastic noise from the post-optimisation expectation value induced by estimating the expectation value with shots. The results are shown in Figs. 20 to 23. We observe that $\alpha_{\text{mean}}^{k\%}$ for the maxbias initial state generally increases with n and l —this is expected as the feasible region size increases, but the number of optimisation steps is fixed. On the contrary, for the warm-started initial state $\alpha_{\text{mean}}^{k\%}$ decreases with n and l . This is because as l is increased, the DGVMP becomes a closer and closer approximation to the GVMP, and thus the warm-started initial state approaches the global minimum. However, the decrease in $\alpha_{\text{mean}}^{k\%}$ with n is an artefact of post-selecting out covariance matrices for which the warm-started initial state is not the DGVMP solution.

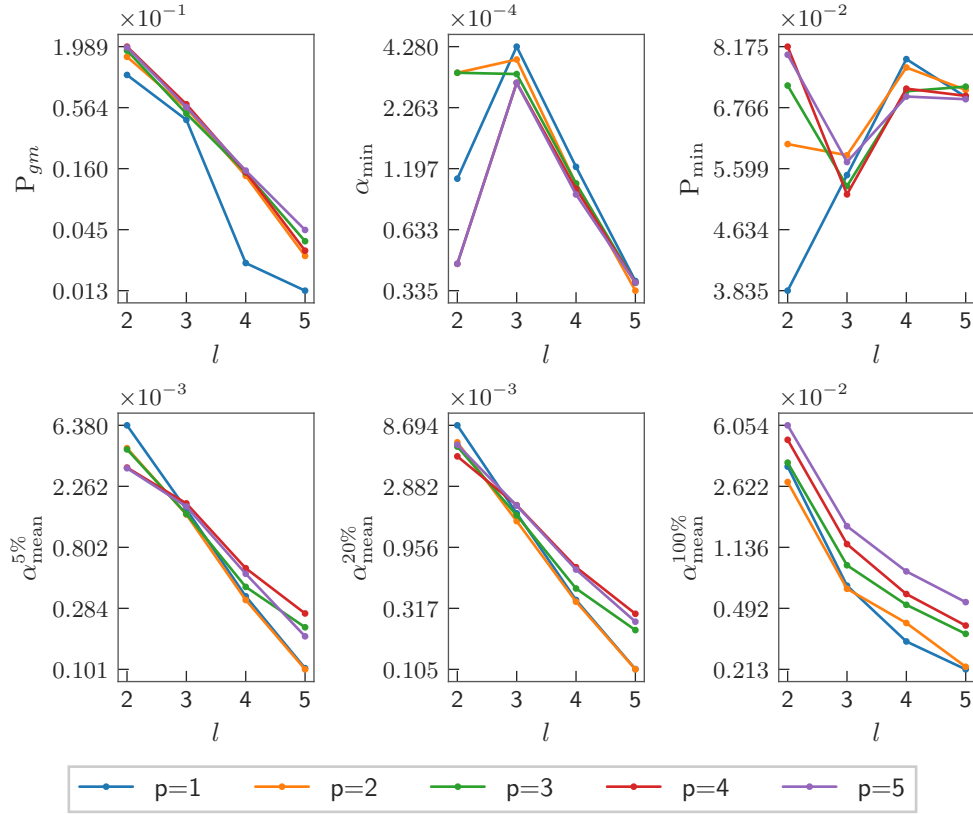


Figure 20. Stochastic simulations of 100 randomly generated DGMVP instances as a function of binary block lengths l with fixed asset size $n = 4$. The initial state is chosen as $|\mathbf{w}\rangle_{ws}$. The top three panels from left to right are the probability of measuring the DGMVP solution P_{gm} , the minimal approximation ratio α_{\min} , and the probability of measuring the minimal value P_{\min} . The bottom three panels from left to right are the 5, 20, and 100 percentile of the mean approximation ratio, respectively.

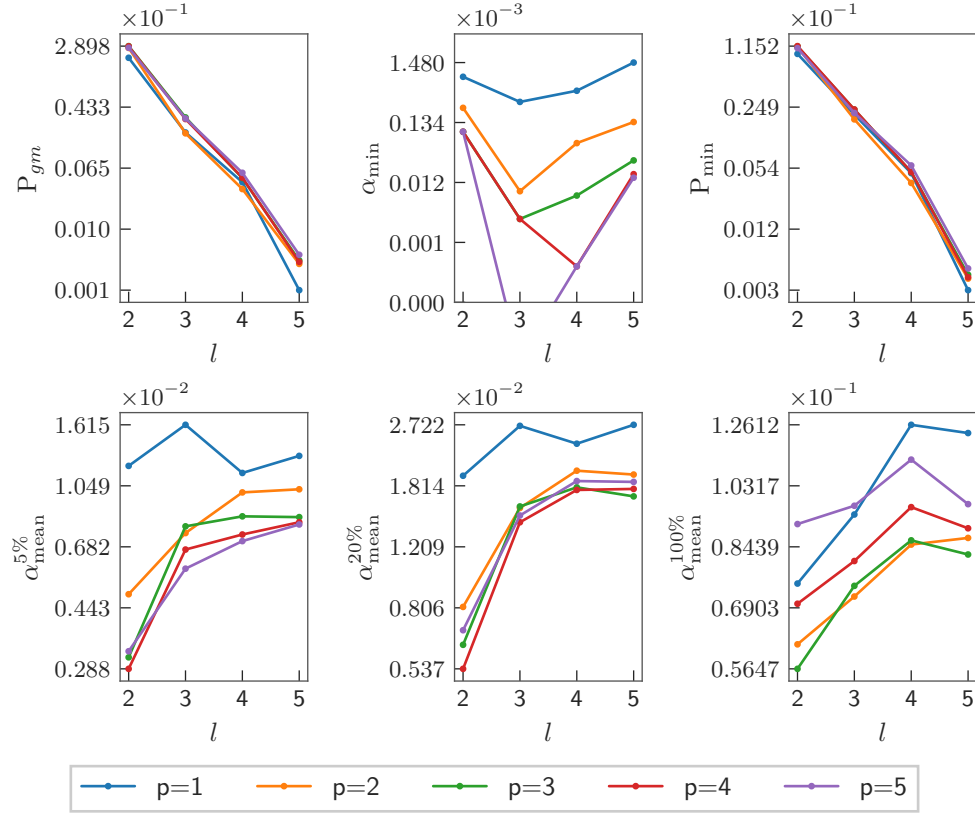


Figure 21. Stochastic simulations of 100 randomly generated DGMVP instances as a function of binary block lengths l with fixed asset size $n = 4$. The initial state is chosen as $|\mathbf{w}\rangle_{mb}$. The top three panels from left to right are the probability of measuring the DGMVP solution P_{gm} , the minimal approximation ratio α_{\min} , and the probability of measuring the minimal value P_{\min} . The bottom three panels from left to right are the 5, 20, and 100 percentile of the mean approximation ratio, respectively.

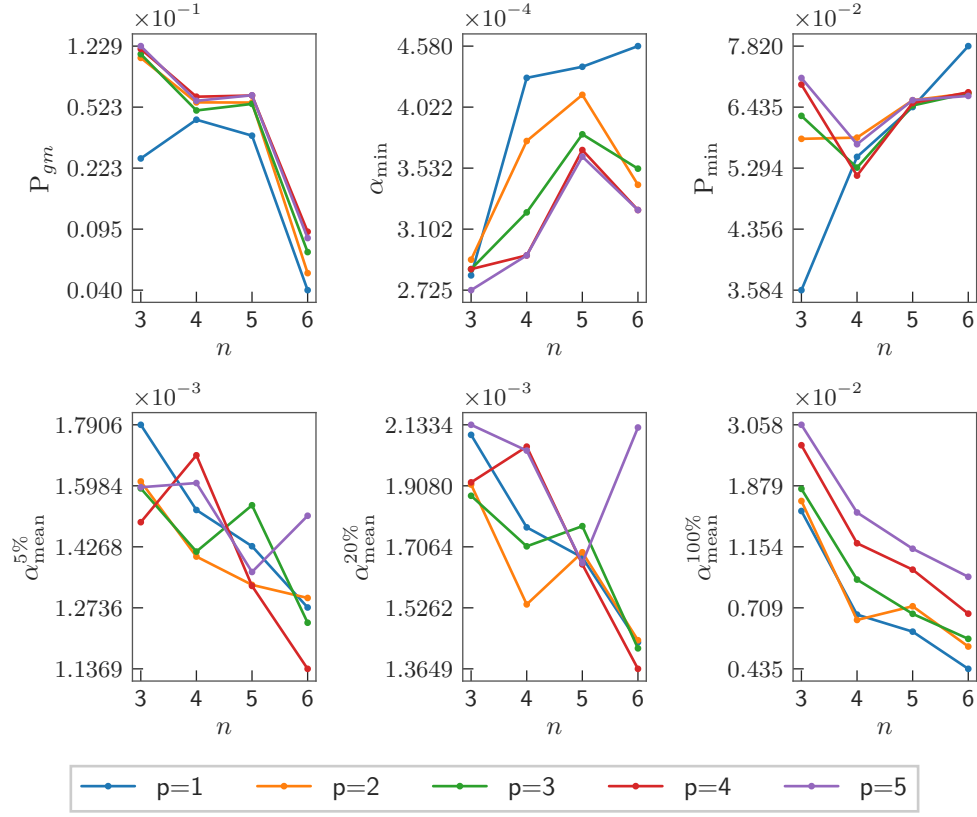


Figure 22. Stochastic simulations of 100 randomly generated DGMVP instances as a function of binary block lengths n with fixed asset size $l = 3$. The initial state is chosen as $|\mathbf{w}\rangle_{ws}$. The top three panels from left to right are the probability of measuring the DGMVP solution P_{gm} , the minimal approximation ratio α_{min} , and the probability of measuring the minimal value P_{min} . The bottom three panels from left to right are the 5, 20, and 100 percentile of the mean approximation ratio, respectively.

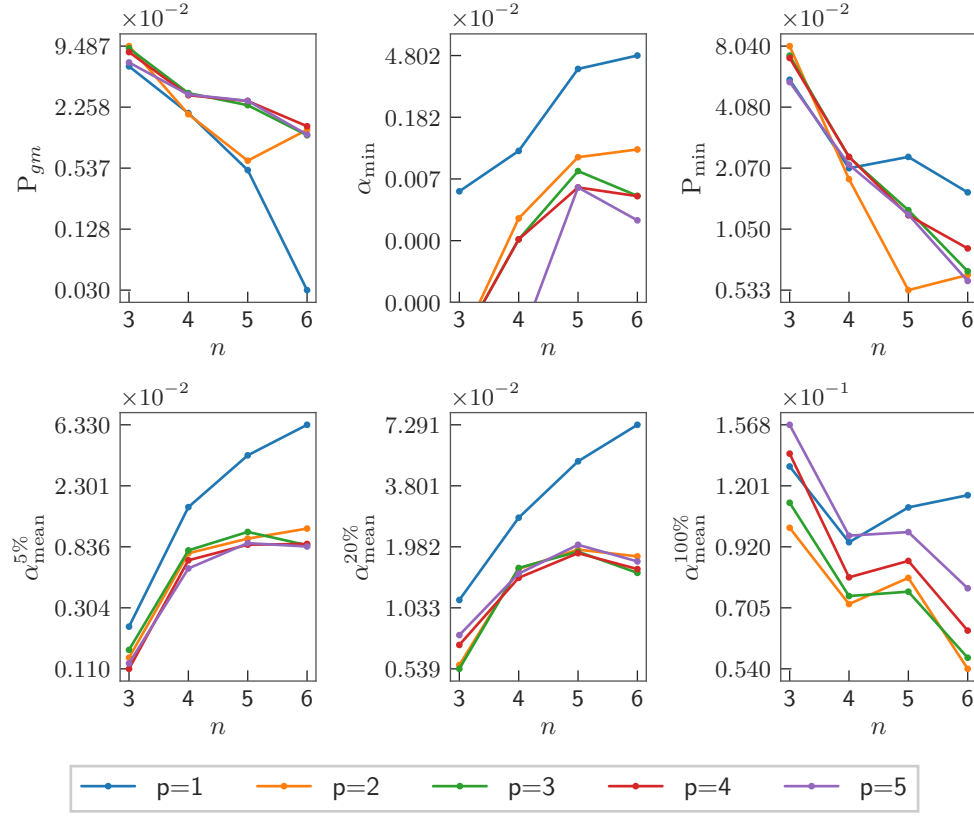


Figure 23. Stochastic simulations of 100 randomly generated DGMVP instances as a function of binary block lengths n with fixed asset size $l = 3$. The initial state is chosen as $|\mathbf{w}\rangle_{mb}$. The top three panels from left to right are the probability of measuring the DGMVP solution P_{gm} , the minimal approximation ratio α_{min} , and the probability of measuring the minimal value P_{min} . The bottom three panels from left to right are the 5, 20, and 100 percentile of the mean approximation ratio, respectively.